



HAL
open science

Dynamics of piezoelectric structures with geometric nonlinearities: A non-intrusive reduced order modelling strategy

Arthur Givois, Jean-François Deü, Olivier Thomas

► **To cite this version:**

Arthur Givois, Jean-François Deü, Olivier Thomas. Dynamics of piezoelectric structures with geometric nonlinearities: A non-intrusive reduced order modelling strategy. *Computers & Structures*, 2021, 253, pp.106575. 10.1016/j.compstruc.2021.106575 . hal-03500725

HAL Id: hal-03500725

<https://cnam.hal.science/hal-03500725>

Submitted on 22 Sep 2022

HAL is a multi-disciplinary open access archive for the deposit and dissemination of scientific research documents, whether they are published or not. The documents may come from teaching and research institutions in France or abroad, or from public or private research centers.

L'archive ouverte pluridisciplinaire **HAL**, est destinée au dépôt et à la diffusion de documents scientifiques de niveau recherche, publiés ou non, émanant des établissements d'enseignement et de recherche français ou étrangers, des laboratoires publics ou privés.



Distributed under a Creative Commons Attribution - NonCommercial 4.0 International License

Dynamics of piezoelectric structures with geometric nonlinearities: A non-intrusive reduced order modelling strategy

Arthur Givois^{a,b}, Jean-François Deü^b, Olivier Thomas^{a,*}

^aArts et Metiers Institute of Technology, LISPEN, HESAM Université, F-59000 Lille, France

^bConservatoire National des Arts et Métiers, Laboratoire de Mécanique des Structures et des Systèmes Couplés (LMSSC), HESAM Université, 2 rue Conté, 75003 Paris, France

A B S T R A C T

A reduced-order modelling to predictively simulate the dynamics of piezoelectric structures with geometric nonlinearities is proposed in this paper. A formulation of three-dimensional finite element models with global electric variables per piezoelectric patch, and suitable with any commercial finite element code equipped with geometrically nonlinear and piezoelectric capabilities, is proposed. A modal expansion leads to a reduced model where both nonlinear and electromechanical coupling effects are governed by modal coefficients, identified thanks to a non-intrusive procedure relying on the static application of prescribed displacements. Numerical simulations can be efficiently performed on the reduced modal model, thus defining a convenient procedure to study accurately the nonlinear dynamics of any piezoelectric structure. A particular focus is made on the parametric effect resulting from the combination of geometric nonlinearities and piezoelectricity. Reference results are provided in terms of coefficients of the reduced-order model as well as of dynamic responses, computed for different test cases including realistic structures.

1. Introduction

The dynamics of piezoelectric systems has been the focus of a large and still increasing amount of studies in the last few decades. Indeed, predicting the dynamics of piezoelectric systems is relevant for numerous applications, such as energy harvesting [1,2], Micro-Electro-Mechanical Systems (MEMS) [3] and vibration reduction using shunt damping [4,5] or active control [6]. More recently, a particular focus has been made on the nonlinear effects to improve the efficiency of electromechanical systems [7–11].

Two main sources of nonlinearities can influence the dynamical behaviour of thin piezoelectric structures. Firstly, the geometric nonlinearities arise in the case of large transverse displacements, creating a significant stretching in the plane of the structure known as the bending-membrane coupling phenomenon [12–16]. More complex nonlinearities, that stem from the large rotations of the structure cross-sections, can also be observed [17,18]. Secondly, material nonlinearities can occur when piezoelectric patches are subjected to high electrical drives, an effect that was investigated on several occasions (see for instance [19–23]). The present paper is devoted to geometrical nonlinearities

only, identified as the predominant ones in some experimental investigations on MEMS with piezoelectric transduction [24–26].

Piezoelectric structures in real-life applications can present complex geometries, often laminated with several layers of different materials [27–29]. Thus, their modelling often relies on the use of a finite element code, which requires a specific electromechanically coupled variational formulation. Since the pioneering proposition in the 70's [30], extensive studies were devoted to the development of piezoelectric finite elements (see among others [31,32], or the reviews [33,34]). Indeed, a large variety of laminated thin-walled piezoelectric elements (beams, plates, shells) with specific kinematics have been introduced (see [35–37] among others). However, these coupled electromechanical formulations are rarely included in commercial finite element codes, in particular when geometrically nonlinear problems are addressed. This justifies the 3D formulation developed in this paper, in order to take a broad-scope approach without restraining to specific structural finite elements. Moreover, such an approach can be addressed with standard commercial finite element codes including both piezoelectric coupling effects and geometrically nonlinear capabilities [38,39].

In order to connect the piezoelectric structure to an electronic circuit, it is convenient to consider global electric variables on the piezoelectric patches (voltage and current/charge), instead of

* Corresponding author.

E-mail address: olivier.thomas@ensam.eu (O. Thomas).

the standard local electric variables used in most finite element formulations. It can be performed thanks to a condensation of the electric degrees of freedom internal to the piezoelectric patches, and by exploiting the equipotentiality properties of the electrodes [40]. It is also possible to express explicitly the global electric variables if the piezoelectric patches are assumed to be thin [41]. Such procedures were initially proposed for linear structures and are here extended to the case of geometrical nonlinearities.

By using direct time integration, simulating the dynamics of a full finite element model presents a high computational cost, even in the linear case [42]. To reduce the number of variables without losing accuracy, reduced-order modelling based on a modal approach was proposed at several occasions. In this case, the linear modal piezoelectric coupling is expressed with only one coefficient per mode, called the modal Electro-Mechanical Coupling Factor (EMCF), identified as the key parameter of the reduced-order modelling procedure [41,43–45]. To estimate this parameter, the more common method relies on the estimation of an effective EMCF obtained thanks to the natural frequencies with the piezoelectric patches in short and in open circuits [46]. However, this method is based on a modal truncation valid if natural frequencies are widely spaced. Another method to compute the EMCF without restrictive assumption has been recently proposed, by computing the global electric charge with short-circuited electrodes in reaction to the modal displacement [47].

In the geometrically nonlinear case, reduced-order models (ROMs) have also been the focus of intensive studies for elastic structures in the past two decades [14]. A natural strategy is a simple expansion on a truncated linear modal basis, with the ROM coefficients efficiently estimated by an enforced displacement method (the so-called STiffness Evaluation Procedure (STEP) [12]). However, the truncation of the modal basis is an issue since a large number of eigenmodes is often required in the basis to obtain converged dynamic solutions. In particular, the coupling between low frequency bending modes and high frequency modes associated with in-plane [48,15] or thickness [49] motions must be taken into account. Many strategies were proposed to overcome this issue, among which: static condensation methods [50,49], modal derivatives and quadratic manifolds [51,52], dual modes [53], spectral submanifolds [54] or invariant manifolds [55–57]. A series of recent studies compare those methods and promote the use of normal form reductions [58,59,56,57,60]. Most of those methods are non-intrusive since they are based on the direct use of output results of a commercial finite element code equipped with geometrically nonlinear capabilities, as opposed to direct methods which require computations implemented at the level of the element [61].

The focus of the present study is to address both geometric nonlinearities and piezoelectricity, for ROMs obtained with a non-intrusive approach. This has been addressed only at three occasions in the literature, to the knowledge of the authors. A first study was based on a home-made finite element code with beam elements [48]. The present paper is a natural extension of this investigation, additionally allowing for the predictive modelling of arbitrary geometries. The second one proposes a method relying on the use of a commercial finite element code, by founding on a thermoelastic analogy [62]. This has the advantage of relying on a convenient non-intrusive approach. However, this analogy only partially accounts for the three-dimensional and the reversibility nature of the piezoelectric constitutive law. Finally, a recent contribution [63] proposes simulations of the resonant nonlinear behaviour of micromirrors under piezoelectric actuation, including nonlinear geometrical effects. A home made finite element code is used with the harmonic balance method, without model order reduction. The combined effects of both piezoelectric and geomet-

rically nonlinear effects results potentially in parametric resonances. Thus, their accurate modelling can lead to efficient predictive simulations of nonlinear vibrations with parametric excitation. This phenomenon was addressed in a large number of studies in the MEMS community (see [25] and references therein) for increasing the quality factor of thin piezoelectric MEMS for which strong nonlinear responses were obtained.

In this overall context, for an elastic structure with piezoelectric elements, the present paper focuses on four main aspects. The first one is concerned with a generic formulation of a 3D finite element (FE) discretized model, that includes both geometric nonlinearities and electromechanical coupling, with global electric variables (voltage and electrode charges). We address secondly the associated modal model, which is reduced around a given resonance by static condensation of the higher order slave modes. Then, the modified STEP (M-STEP) method, introduced in [49] for elastic structures, is extended to a piezoelectric structure, to efficiently compute the electromechanical coefficients of the ROM, in the case of a symmetric structure in the transverse direction. Finally, the ROM is validated by comparison to analytical solutions and full 3D FE computations, thanks to dynamic responses in the frequency domain. One of the main originality is the emergence of special terms in the formulation, due to the conjugate effect of piezoelectricity and geometrical nonlinearities, and physically responsible for parametric excitation and instabilities of thin symmetric structures. Another originality is the systematic consideration of both converse (actuation) and direct (detection) piezoelectric effects.

2. Finite element formulation of the geometrically nonlinear problem with piezoelectric patches

2.1. Notations and assumptions

A piezoelectric structure is considered in its reference configuration as defined in Fig. 1. It occupies a domain Ω , of boundary $\partial\Omega$, of the three-dimensional Euclidean space. It is subjected to a prescribed displacements u_i^d on a part $\partial\Omega_u$ of its boundary $\partial\Omega$, whereas a surface force density t_i^d is applied on the complementary part $\partial\Omega_t$. Note that subscripts i, j, l, k denote the three-dimensional vector and tensor components and repeated subscripts imply summation, according to standard indicial notations. Similarly, the electric boundary conditions are defined by a prescribed electric potential ψ^d on $\partial\Omega_\psi$ and a prescribed boundary charge density q^d on the remaining part $\partial\Omega_q$. These boundaries are consequently organized such that $\partial\Omega = \partial\Omega_t \cup \partial\Omega_u = \partial\Omega_q \cup \partial\Omega_\psi$, and $\partial\Omega_t \cap \partial\Omega_u = \partial\Omega_q \cap \partial\Omega_\psi = \emptyset$. Moreover, body forces of density b_i^d are applied in Ω .

Let Y_i and y_i be the position vector in the reference and actual configurations, respectively. The equations governing the mechanical state are written in terms of the structural mechanical displacements $u_i = y_i - Y_i$, whereas the electric state is expressed in terms of the electric potential ψ . Since a Lagrangian formulation is used, they are both expressed in the reference configuration.

The structure consists of an elastic part of domain Ω_{el} , equipped with P piezoelectric patches of index p with $p \in [1, \dots, P]$ occupying domains Ω_p , such that the domain set $(\Omega_{el}, \Omega_1, \Omega_2, \dots, \Omega_p)$ is a partition of Ω . The constitutive behaviour of the materials is assumed to be linear and includes the piezoelectric effect. Note that the piezoelectric constants are zero in Ω_{el} . The patches are covered on their upper and lower surfaces with layers of conducting material to obtain electrodes. The piezoelectric patches are polarized in their transverse direction, *i.e.* along the normal to the electrodes, and the free charges are localized in the common surface of the patches and the electrodes. The thickness of the electrode can be

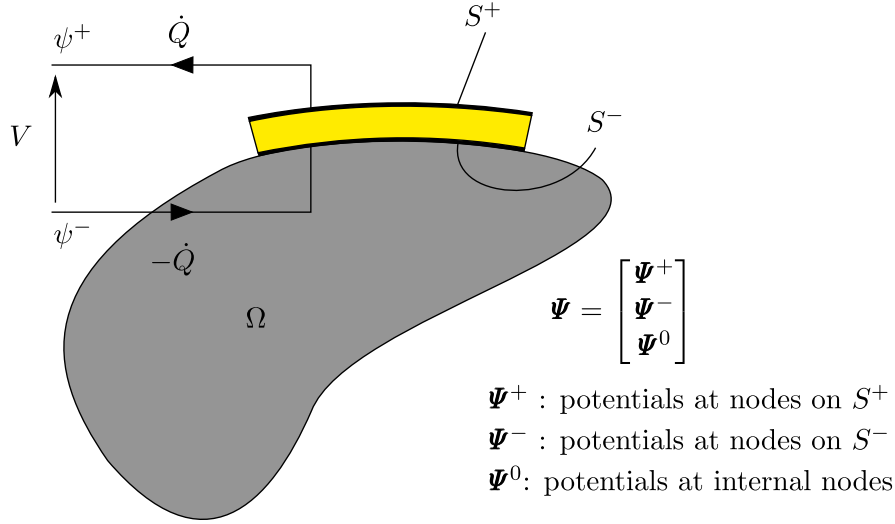


Fig. 1. Scheme of a whole piezoelectric structure with one patch. Elastic and piezoelectric materials are respectively represented in grey and yellow. (For interpretation of the references to colour in this figure legend, the reader is referred to the web version of this article.)

neglected for some applications [41], or the electrode can be included in the 3D model as an additional elastic layer [27].

2.2. Strong formulation

We introduce the deformation gradient tensor $F_{ij} = \partial y_i / \partial Y_j = \delta_{ij} + u_{i,j}$, where δ is the Kronecker delta. The strong form of the mechanical problem expressed with respect to the reference configuration writes [64]:

$$(F_{ij}S_{jk})_{,k} + b_i^d = \rho \ddot{u}_i \quad \text{in } \Omega \quad (1a)$$

$$F_{ij}S_{jk}n_k = t_i^d \quad \text{on } \partial\Omega_t \quad (1b)$$

$$u_i = u_i^d \quad \text{on } \partial\Omega_u. \quad (1c)$$

In these equations, ρ denotes the mass density, S_{jk} the second Piola–Kirchhoff stress tensor, n_k is the unit normal external to $\partial\Omega_t$. Moreover, the space and time derivatives are respectively denoted by $\bullet_{,k} = \partial \bullet / \partial Y_k$ and $\dot{\bullet} = \partial \bullet / \partial t$. Using electrostatic assumptions, the strong formulation of the electrical problem writes, in the reference configuration [65, §4.4]:

$$D_{i,i} = 0 \quad \text{in } \Omega, \quad (2a)$$

$$D_i n_i = -q^d \quad \text{on } \partial\Omega_q, \quad (2b)$$

$$\psi = \psi^d \quad \text{on } \partial\Omega_\psi. \quad (2c)$$

where D_i denotes the electric displacement vector expressed in the reference configuration. Eqs. (1) and (2) are the local equations of the electromechanical problem. In particular, Eq. (1a) is the elastodynamic equation, Eq. (2a) is the Gauss's law and Eqs. (1b), (1c), (2b) and (2c) are the mechanical and electrical boundary conditions.

For the constitutive law, we consider that the local strains are small, which justifies using a fully linear relation between the Lagrangian variables [66, §6]. It takes the form of a Saint–Venant–Kirchhoff law with a linear piezoelectric coupling, which reads:

$$S_{ij} = c_{ijkl}^E \varepsilon_{kl} - e_{kij} E_k \quad (3a)$$

$$D_i = e_{ikl} \varepsilon_{kl} + \epsilon_{ik}^E E_k, \quad (3b)$$

where c_{ijkl}^E is the fourth-order tensor of elasticity at constant electric field, e_{ikl} is the third-order tensor of piezoelectric constants verifying $e_{ijk} = 0$ in Ω_s and ϵ_{ik}^E is the tensor of dielectric permittivities at

constant strain. ε_{ij} denotes the Green–Lagrange strain tensor, given by:

$$\varepsilon_{ij} = \frac{1}{2} (u_{i,j} + u_{j,i} + u_{k,i} u_{k,j}). \quad (4)$$

Finally, E_i is the electric field in the reference configuration, related to the electric potential by:

$$E_i = -\psi_{,i}. \quad (5)$$

2.3. Weak formulation

The test-function method is applied to state the weak formulation of the electromechanical problem. We introduce the spaces \mathcal{C}_u of sufficiently regular functions u_i defined in Ω , \mathcal{C}_ψ the spaces of sufficiently regular functions ψ , $\mathcal{C}_u^* = \{u_i \in \mathcal{C}_u | u_i = 0 \text{ on } \partial\Omega_u\}$ and $\mathcal{C}_\psi^* = \{\psi \in \mathcal{C}_\psi | \psi = \psi^d \text{ on } \partial\Omega_\psi\}$. After multiplying Eqs. (1) and (2) respectively by any time-independent test functions $\delta u_i \in \mathcal{C}_u^*$ and $\delta \psi \in \mathcal{C}_\psi^*$, applying the divergence theorem and using Eqs. (1b), (2b) and (3), we obtain the following weak formulation for the electrical problem:

$$\int_{\Omega} c_{ijkl}^E \varepsilon_{kl}(u) \delta \varepsilon_{ij}(u, \delta u) d\Omega - \int_{\Omega} e_{kij} E_k(\psi) \delta \varepsilon_{ij}(u, \delta u) d\Omega + \int_{\Omega} \rho \ddot{u}_i \delta u_i d\Omega = \int_{\Omega} b_i^d \delta u_i d\Omega + \int_{\partial\Omega_t} t_i^d \delta u_i dS \quad \forall \delta u_i \in \mathcal{C}_u. \quad (6a)$$

$$\int_{\Omega} e_{ikl} \varepsilon_{kl}(u) \delta E_i(\delta \psi) d\Omega + \int_{\Omega} \epsilon_{ik}^E E_k(\psi) \delta E_i(\delta \psi) d\Omega = \int_{\partial\Omega_q} q^d \delta \psi dS + \int_{\partial\Omega_\psi} q^r \delta \psi dS \quad \forall \delta \psi \in \mathcal{C}_\psi \quad (6b)$$

with $q^r = -D_i n_i$ the reactive nodal charge on $\partial\Omega_\psi$. Eqs. (6a) and (6b) correspond to the equality of the virtual works, respectively for the mechanical part and for the electrical part.

2.4. Finite element discretization

Equations. (6a) and (6b) are now used to obtain a finite element discretization of the problem. Considering a standard three-dimensional discretization and defining (U_j, Ψ_k) the nodal unknowns, respectively the displacement and the electric poten-

tial, the general finite element formulation can be written (see A for details):

$$M_{ij}\ddot{U}_j + K_{ij}^m U_j + f_i^m(U) + [K_{ik}^c + L_{ikm}^c U_m] \Psi_k = f_i^{\text{ext}} \quad (7a)$$

$$K_{kl}^e \Psi_l - \left[K_{ki}^c + \frac{1}{2} L_{kim}^c U_m \right] U_i = q_k, \quad (7b)$$

where M_{ij} and K_{ij}^m denote the mass and mechanical stiffness matrices, $f_i^m(U)$ the nonlinear internal force vector, K_{ik}^c and L_{ikm}^c the linear and nonlinear electromechanical coupling matrices, and K_{kl}^e is the dielectric matrix. Finally, f_i^{ext} and q_k correspond respectively to the mechanical forcing and to the electric charge on the boundaries. $M_{ij}, K_{ij}^m, K_{kl}^e$ and K_{ik}^c are symmetric matrices.

The above finite element formulation is the one that is used in most finite element codes with both geometrical nonlinearities and piezoelectric capabilities [38,39]. It shows that the geometrical nonlinearities and the piezoelectric effect appear through three additive groups of terms:

- geometrically nonlinear effects are embedded in the nonlinear internal force vector $f_i^m(U)$. It includes quadratic and cubic terms such that it can be written $f_i^m(U) = K_{ijl}^{(2)} U_j U_l + K_{ijlm}^{(3)} U_j U_l U_m$, with $K_{ijl}^{(2)}$ and $K_{ijlm}^{(3)}$ the quadratic and cubic stiffness matrices defined in A. This nonlinear part was investigated at numerous occasions [64,14,67,68]. It appears naturally if the structure is considered purely elastic, by setting $\Psi_k = 0$ everywhere in the domain Ω , in the case of a geometrically nonlinear computation without piezoelectric effects;
- K_{ik}^c is the matrix that couples linearly electrical and mechanical degrees of freedom, that emerges in any linear piezoelectric computation (without geometrical nonlinearities, i.e. with $f_i^m(U) = L_{ikm}^c = 0$). A large literature is devoted to this effect, see for instance [30,33,43,41].
- L_{ikm}^c corresponds to a third-order tensor which stems from the combined effect of piezoelectricity and geometric nonlinearities. This term was little addressed in the past (see [62,48]). Its investigation is then a key point of the present paper. It should be stressed that this term is half as small in the electrical equation (Eq. (7b)) as it is in the mechanical one (Eq. (7a)), due to the doubling of the non-linear terms in the variation of the strains (see Eq. (A.1)). Although this term was originally presented in [48], the half factor in the electrical equation was missed. The tensor presents also the symmetry property $L_{ikm}^c = L_{mki}^c$. The interested reader is referred to A for the justification of these properties. In Eq. (7a), the term $L_{ikm}^c \Psi_k$, multiplied by the displacement U_m , can be viewed as a mechanical stiffness that is proportional to the electric potential Ψ_k . Then, if the piezoelectric patches are used as actuators, for which the electrical state is prescribed by an external source, the term $L_{ikm}^c \Psi_k$ can be the source of a parametric excitation of the structure (see e.g. [25]). L_{ikm}^c will then be denoted as the ‘‘parametric’’ tensor in the following.

2.5. Global electric degrees of freedom

To easily connect the model to an electric circuit, Eqs. (7) are rewritten by condensing the electric degrees of freedom internal to the P piezoelectric patches and by taking into account the equipotentiality properties in the electrodes. This procedure, already proposed in many papers [69,70,40,43], is here generalized with geometric nonlinearities. The corresponding derivations are reported in B. With this condensation, Eqs. (7) are rewritten:

$$M\ddot{\mathbf{U}} + \mathbf{f}^{\text{int}}(\mathbf{U}) + \sum_{p=1}^P [\mathbf{f}_c^{(p)} + \mathbf{P}_c^{(p)} \mathbf{U}] V^{(p)} = \mathbf{f}^{\text{ext}} \quad (8a)$$

$$C^{(p)} V^{(p)} - \left[\mathbf{f}_c^{(p)} + \frac{1}{2} \mathbf{P}_c^{(p)} \mathbf{U} \right]^T \mathbf{U} = Q^{(p)} \quad \forall p \in [1, P], \quad (8b)$$

where, for the p -th. piezoelectric patch, $(V^{(p)}, Q^{(p)})$ denote respectively the voltage between the electrodes and the electric charge contained in one of the electrodes and $C^{(p)}$ its electric capacitance. It is assumed that no electrostatic coupling was observed between the piezoelectric patches, which results in no other capacitances than the $C^{(p)}$.

The modified internal force vector reads:

$$\mathbf{f}^{\text{int}}(\mathbf{U}) = \mathbf{K}\mathbf{U} + \mathbf{f}(\mathbf{U}) \quad (9)$$

with \mathbf{K} and \mathbf{f} the linear stiffness matrix and the nonlinear internal force vector, that differ from \mathbf{K}^m and \mathbf{f}^m because of the condensation of the electrical potential. Finally, the linear and nonlinear electromechanical coupling vector and matrix are respectively denoted with $\mathbf{f}_c^{(p)}$ and $\mathbf{P}_c^{(p)}$ after this condensation. Explicit expressions of $\mathbf{K}, \mathbf{f}, \mathbf{f}_c^{(p)}$ and $\mathbf{P}_c^{(p)}$ are provided in Eq. (B.3). These expressions show that the symmetry property of the parametric matrix is preserved, such that $\mathbf{P}_c^{(p)T} = \mathbf{P}_c^{(p)}$. Moreover, Eqs. (7a,b) and (8a,b) share the same structure and thus, analog properties that those stated at the end of Section 2.4 also apply to Eqs. (8a,b).

2.6. Modal expansion

The displacements are now expanded on a basis of N eigenmodes:

$$\mathbf{U}(t) = \sum_{k=1}^N \Phi_k X_k(t) \quad (10)$$

with $X_k(t)$ the modal coordinates of the k^{th} mode. ω_k and Φ_k are respectively the eigenvalues and eigenvectors of the free linearized and short-circuited counterpart of Eqs. (8):

$$(\mathbf{K} - \omega_k^2 \mathbf{M}) \Phi_k = \mathbf{0}. \quad (11)$$

Introducing Eq. (10) into Eqs. (8), multiplying (8a) by Φ_k^T and using the orthogonality property of the modes leads to, for all $k = 1, \dots, N, p = 1, \dots, P$:

$$\ddot{X}_k + \omega_k^2 X_k + \sum_{i=1}^N \sum_{j=i}^N a_{ij}^k X_i X_j + \sum_{i=1}^N \sum_{j=i}^N \sum_{l=j}^N b_{ijl}^k X_i X_j X_l + \sum_{p=1}^P \chi_k^{(p)} V^{(p)} + \sum_{p=1}^P \sum_{i=1}^N \Theta_{ik}^{(p)} X_i V^{(p)} = F_k, \quad (12a)$$

$$C^{(p)} V^{(p)} - \sum_{k=1}^N \chi_k^{(p)} X_k - \sum_{i=1}^N \sum_{j=1}^N \frac{1}{2} \Theta_{ij}^{(p)} X_i X_j = Q^{(p)}, \quad (12b)$$

with the modal forcing $F_k = \Phi_k^T \mathbf{f}^{\text{ext}} / m_k$ and the modal mass $m_k = \Phi_k^T \mathbf{M} \Phi_k$ of the k -th. mode. In all the numerical examples of Sections 5 and 6, the mode shapes are mass-normalized ($m_k = 1$ for all k). It leads to particular units for the quantities in the modal model: $\text{kg}^{-1/2}$ for the displacement components of Φ_k , $\text{m kg}^{1/2}$ for X_k , $\text{N kg}^{-1/2}$ for F_k , $\text{N m}^{-2} \text{kg}^{-3/2}$ for a_{ij}^k , $\text{N m}^{-3} \text{kg}^{-2}$ for b_{ijl}^k , $\text{N V}^{-1} \text{kg}^{-1/2}$ for $\chi_k^{(p)}$, $\text{N m}^{-1} \text{V}^{-1} \text{kg}^{-1}$ for $\Theta_{ik}^{(p)}$. The units of V and Q are standard, respectively V and C.

In Eqs. (12a,b), in the same manner than for Eqs. (7) and (8), one can observe analogous groups of terms and mention the following comments about the coefficients of the modal expansion:

- the coefficients a_{ij}^k and b_{ij}^k are quadratic and cubic coefficients stemming from the geometric nonlinearities;
- $\chi_k^{(p)}$ are the linear electromechanical modal coupling coefficients defined by $\chi_k^{(p)} = \Phi_k^T \mathbf{f}_c^{(p)}$. They are the key parameters for the efficiency of the piezoelectric structure, as pointed out in other investigations [43,41,45,47].
- $\Theta_{ik}^{(p)}$ are the quadratic electromechanical modal coupling coefficients defined by $\Theta_{ik}^{(p)} = \Phi_k^T \mathbf{P}_c^{(p)} \Phi_i$. A particular focus is here made on these original coefficients, which are responsible for parametric excitation in piezoelectric structures [48]. It should be noted that $\Theta_{ik}^{(p)} = \Theta_{ki}^{(p)}$ since $\mathbf{P}_c^{(p)}$ is symmetric.

The above model is generic for any elastic structure with geometrical nonlinearities and piezoelectric coupling. In practice, one selects a small number N of retained modes, which can significantly reduce the size of this modal expansion as compared to the one of the initial finite element model. Some examples will be given in Sections 5 and 6. However, a potentially large number of coefficients $a_{ij}^k, b_{ij}^k, \chi_k^{(p)}$ and $\Theta_{ik}^{(p)}$ remains to be computed, an issue addressed in the two following sections.

3. Identification of the modal model

This section focuses on the computation of the coefficients of Eqs. (12). The linear parameters ω_k, Φ_k and F_k are directly computed by the modal analysis of Eq. (11), available in any finite element code. We focus here on the computation of the coefficients $a_{ij}^k, b_{ij}^k, \chi_k^{(p)}$ and $\Theta_{ik}^{(p)}$ and the capacitances $C^{(p)}$. Since the three main corresponding effects are additively written, we propose here to compute these different coefficients separately. Indeed, if short-circuited piezoelectric patches are prescribed, all coupling terms due to piezoelectricity vanish in Eqs. (12), which is then equivalent to an elastic model with geometric nonlinearities. Conversely, if geometric nonlinearities are turned off, Eqs. (12) becomes a piezoelectric linear model. After studying these two separated problems, parametric effects can be investigated by activating both geometric nonlinearities and piezoelectricity and keeping all terms of Eqs. (12).

We thus adopt a four steps approach to compute the parameters of the reduced-order model. For each step, a non-intrusive method is used, relying on prescribing static displacements having the shape of selected eigenmodes with a given amplitude, as first introduced by Muravyov and Rizzi [12] and called STEP (STiffness Evaluation Procedure). The idea of this method is that an appropriate choice of the selected eigenmodes and respective amplitudes leads to a simple algebra, which allows for computing the coefficients from the internal force vector and the electric charge given by the finite element code.

The first step is the computation of the nonlinear coefficients a_{ij}^k and b_{ij}^k . Since it is classical, the interested reader can refer to [71,14,15,49] for details. It is performed here with the electrodes short-circuited. The two following step are related to the computation of the electromechanical coefficients $\chi_k^{(p)}$ and $\Theta_{ik}^{(p)}$. In the following sections, we propose an original use of the STEP for computing the electromechanical coefficients $\chi_k^{(p)}$ and $\Theta_{ik}^{(p)}$. Then, the last step is the computation of the capacitances $C^{(p)}$.

3.1. Computation of the linear electromechanical coefficients $\chi_k^{(p)}$

We propose to identify the coefficients $\chi_k^{(p)}$ by simply using the computation of the eigenmodes in Eq. (11) and of the resulting electric charge on the electrodes of the piezoelectric patches

$p \in [1, \dots, P]$. This method, introduced in [47], can be viewed as an extension of the STEP to compute coefficients. Indeed, the k^{th} eigenvector computed in Eq. (11) is a displacement field equal to the mode shape with a unitary modal coordinate X_k . With Eq. (10), that reads:

$$\mathbf{U} = \Phi_k, \quad \iff \quad X_r = \begin{cases} 1 & \text{if } r = k \\ 0 & \text{if } r \neq k. \end{cases} \quad (13)$$

Since the modal analysis with short-circuited electrodes ($V^{(p)} = 0 \forall p \in [1, \dots, P]$) of Eq. (11) is linear, Eq. (12b) is equivalent to:

$$\chi_k^{(p)} = -Q_k^{(p)}. \quad (14)$$

In practice, $Q_k^{(p)}$ is computed by summing all the nodal charges (the q_k of the second member of Eq. (7b), called ‘‘reactive electrical nodal charge’’ in Abaqus) on the upper electrodes of the p^{th} piezoelectric patch, as stated in Eq. (B.7). Moreover, the short circuit state of the electrodes is prescribed by setting to zero the electric potential at their nodes, naturally ensuring the equipotentiality condition without additional constraint. This method allows to estimate directly the linear coefficients $\chi_k^{(p)}$ of all patches p for a given vibration mode k , by a direct product of the modal analysis.

3.2. Computation of the nonlinear electromechanical coefficients $\Theta_{ik}^{(p)}$

When the linear coupling coefficients $\chi_k^{(p)}$ are known, a procedure relying on the static prescription of eigenmodes is performed to compute the coefficients $\Theta_{ik}^{(p)}$. This extension of the STEP for the computation of piezoelectric coefficients was never proposed before, to the knowledge of the authors.

The coefficients $\Theta_{ii}^{(p)}$ are first computed by prescribing the following time-independent displacement field to the structure:

$$\mathbf{U} = \lambda_i \Phi_i, \quad \iff \quad X_r = \begin{cases} +\lambda_i & \text{if } r = i \\ 0 & \text{if } r \neq i \end{cases} \quad (15)$$

where λ_i is an amplitude coefficient of the eigenvector Φ_i , chosen so as to ensure that geometric nonlinearities are activated [15]. Introducing Eq. (15) in Eq. (12b) with geometric nonlinearities activated in the FE code and short-circuited electrodes leads to:

$$\Theta_{ii}^{(p)} = -\frac{2}{\lambda_i^2} \left(\chi_i^{(p)} \lambda_i + Q_{ii}^{(p)} \right). \quad (16)$$

In this problem, $Q_{ii}^{(p)}$ is computed with the sum of the nodal charges on the upper electrodes of the p^{th} piezoelectric patch (cf. Eq. (B.7)).

Then, the coefficients $\Theta_{ij}^{(p)}$ with $i \neq j$ are identified by expanding the displacement on the modes (i, j) such that:

$$\mathbf{U} = \lambda_i \Phi_i + \lambda_j \Phi_j \quad (17)$$

and computing the resulting charge $Q_{ij}^{(p)}$ from the FE code. By using the property $\Theta_{ij}^{(p)} = \Theta_{ji}^{(p)}$ and Eq. (16), these parametric coefficients are then written:

$$\Theta_{ij}^{(p)} = \Theta_{ji}^{(p)} = -\frac{1}{\lambda_i \lambda_j} \left(Q_{ij}^{(p)} - Q_{ii}^{(p)} - Q_{jj}^{(p)} \right), \quad (18)$$

where $Q_{ij}^{(p)}$ is also obtained by summing of the nodal charges on the upper electrodes of the p^{th} piezoelectric patch.

We showed in this section that once the coefficients $\chi_i^{(p)}$ are known, all parametric coefficients $\Theta_{ij}^{(p)}$ of any modal basis can be computed by solving a set of static computations with the FE code. It should be noted that the static computations with enforced displacements of Eqs. (15) and (17) and short-circuited electrodes

need also to be performed in the classical STEP to identify the non-linear coefficients a_{ij}^k and b_{ijl}^k . Thus, the proposed method only requires the computations of the corresponding electric charges ($Q_{ii}^{(p)}, Q_{ij}^{(p)}, Q_{jj}^{(p)}$, obtained by summing nodal charges on the appropriated electrodes) as additional computations to obtain the electromechanical coefficients $\chi_i^{(p)}$ and $\Theta_{ij}^{(p)}$. Moreover, as in the previous section, the equipotentiality condition in the electrodes is naturally fulfilled with the setting of the electrical potential to zero for all the nodes of the electrodes.

3.3. Computation of the capacitances

The capacitances $C^{(p)}$ of the P piezoelectric patches can be computed by a single computation in the FE code. By prescribing (i) non zero values of the potentials $V^{(p)}, p = 1, \dots, P$, and (ii) a zero displacement to all the degrees of freedom of the structure, $U_i = 0 \Rightarrow X_k = 0$ for all i, k and (iii) computing the resulting charges $Q^{(p)}$ with Eq. (B.7), Eq. (12b) gives $C^{(p)} = Q^{(p)}/V^{(p)}$ for all p . Another possibility, for thin piezoelectric patches of electrode area $S^{(p)}$ and thickness $h^{(p)}$, is to use the formula $C^{(p)} = \epsilon_{33}^e S^{(p)}/h^{(p)}$ where 3 is the direction normal to the electrode.

4. The case of flat structures

The procedure of the previous section can be applied to compute the coefficients related to any modal basis, for any geometry of the electromechanical structure. However, a large number N of eigenmodes can be required in the basis to obtain converged dynamic solutions, especially when 3D finite elements are used, because of the coupling between low frequency bending modes and high frequency modes associated with in-plane [48,15] or thickness [49] motions. As reported in the introduction, several strategies have been developed to overcome this issue in the case of elastic structures. The extension of those techniques to the present case of an electromechanical structure remains to be addressed and we focus here on the validation of the model exposed in the previous sections. For this, we restrict the analysis to the case of flat and symmetric structures, for which a simple extension of the STEP, called the ‘‘modified STEP’’ (M-STEP), has been recently proposed in [49]. This section thus proposes an extension of this work to the case of a piezoelectric structure and enables to efficiently compute the coefficients of a ROM restricted to a few low frequency pure bending modes, with the membrane and thickness motions statically condensed. This will be the starting point of the validations proposed in Section 5. The remaining of the section introduces developments similar to those in [49], included here to develop the treatment of the piezoelectric related terms.

4.1. Bending uncoupling and static condensation

We consider a flat structure, defined by a low aspect ratio ($h/L \ll 1$ with h the thickness and L a characteristic dimension of the structure) and with a symmetric material distribution with regard to the middle line/ plane. In this case, the linear bending-membrane coupling induced by the lamination of the structure is zero [72]. Consequently, the modal basis can be split in two family of eigenmodes. First, the bending modes have mainly transverse non-zero displacements and are present at low frequencies in the spectrum. Secondly, membrane modes present negligible or zero transverse components, as well as natural frequencies outside the frequency band of interest. In addition, with a 3D FE model, thickness modes, that mainly involves cross-section deformations, are also present in this higher part of the spectrum.

As in [49], we assume that the modal coordinates vector $\mathbf{X} = [X_1, \dots, X_N]^T$ can be split in a bending part and a non bending (NB) part, so that $\mathbf{X} = [x_1, x_2, \dots, x_{N_B}, \eta_{N_B+1}, \dots, \eta_N]$ with $x_r, r = 1, \dots, N_B$ the bending modal coordinates and $\eta_s, s = N_B + 1, \dots, N$ the NB modal coordinates. This NB part consists first of axial displacement fields with negligible transverse displacements, and secondly of purely thickness modes with negligible transverse displacement on the middle plane. We suppose that the natural frequencies of NB modes are higher than those of the bending ones, that means $\omega_r \ll \omega_s$ for all $s = N_B + 1, \dots, N$ and $r = 1, \dots, N_B$.

We also assume that the piezoelectric system is mechanically excited by a transverse forcing, such that no mechanical forcing is applied on the NB modes ($F_s = 0 \forall s \in [N_B + 1, \dots, N]$). We also consider that the bending motion is predominant, such that given a small parameter ε , we have $x_r = O(\varepsilon)$ for $r \in [1, \dots, N_B]$ and $\eta_s = O(\varepsilon^2)$ for $s \in [N_B + 1, \dots, N]$. We finally assume that the ‘‘13’’ effect of the piezoelectric material is predominant in the flat structure, which induces that the mechanical effect of the applied voltage is of the same order of magnitude as an in-plane stretching, that means $V^{(p)} = O(\varepsilon^2)$. Introducing this scaling in Eqs. (12a) and keeping only the leading orders conducts to:

$$\begin{aligned} \ddot{x}_k + \omega_k^2 x_k + \sum_{i=1}^{N_B} \sum_{s=N_B+1}^N a_{is}^k x_i \eta_s + \sum_{i=1}^{N_B} \sum_{j=1}^{N_B} \sum_{l=1}^{N_B} b_{ijl}^k x_i x_j x_l \\ + \sum_{p=1}^P \chi_k^{(p)} V^{(p)} + \sum_{p=1}^P \sum_{i=1}^{N_B} \Theta_{ik}^{(p)} x_i V^{(p)} + O(\varepsilon^4) = F_k \\ \ddot{\eta}_s + \omega_s^2 \eta_s + \sum_{i=1}^{N_B} \sum_{j=1}^{N_B} a_{ij}^s x_i x_j + \sum_{p=1}^P \chi_s^{(p)} V^{(p)} + O(\varepsilon^3) = 0 \\ C^{(p)} V^{(p)} - \sum_{i=1}^{N_B} \chi_i^{(p)} x_i - \sum_{s=N_B+1}^N \chi_s^{(p)} \eta_s - \sum_{i=1}^{N_B} \sum_{j=1}^{N_B} \frac{1}{2} \Theta_{ij}^{(p)} x_i x_j + O(\varepsilon^3) = Q^{(p)}. \end{aligned} \quad (19b)$$

Since $\omega_s \gg \omega_k$, the inertia in Eq. (19b) can be neglected, which thus leads to:

$$\eta_s = -\omega_s^{-2} \left(\sum_{i=1}^{N_B} \sum_{j=1}^{N_B} a_{ij}^s x_i x_j + \sum_{p=1}^P \chi_s^{(p)} V^{(p)} \right). \quad (20)$$

Introducing Eq. (20) in Eqs. (19a) and (19c) leads to the following equations, for all $k = 1, \dots, N_B, p = 1, \dots, P$:

$$\begin{cases} \ddot{x}_k + \omega_k^2 x_k + \sum_{i=1}^{N_B} \sum_{j=1}^{N_B} \sum_{l=1}^{N_B} \Gamma_{ijl}^k x_i x_j x_l + \sum_{p=1}^P \chi_k^{(p)} V^{(p)} + \sum_{p=1}^P \sum_{i=1}^{N_B} \Lambda_{ik}^{(p)} x_i V^{(p)} + O(\varepsilon^4) = F_k, & (a) \\ C^{(p)} V^{(p)} + \sum_{s=N_B+1}^N \sum_{i=1}^{N_B} \frac{\chi_i^{(p)} \omega_i^2}{\omega_s^2} V^{(e)} - \sum_{i=1}^{N_B} \chi_i^{(p)} x_i - \sum_{i=1}^{N_B} \sum_{j=1}^{N_B} \frac{1}{2} \Lambda_{ij}^{(p)} x_i x_j + O(\varepsilon^3) = Q^{(p)}, & (b) \end{cases} \quad (21)$$

with Γ_{ijl}^k the condensed cubic coefficients already introduced in [49] and $\Lambda_{ik}^{(p)}$ the condensed parametric coefficients, respectively defined by:

$$\Gamma_{ijl}^k = b_{ijl}^k - \sum_{s=N_B+1}^N \mathcal{C}_{ijl}^{ks} \quad (22a)$$

$$\Lambda_{ik}^{(p)} = \Theta_{ik}^{(p)} - \sum_{s=N_B+1}^N \mathcal{F}_{ik}^{s(p)}, \quad \mathcal{F}_{ik}^{s(p)} = \frac{\chi_s^{(p)} a_{ik}^s}{\omega_s^2}. \quad (22b)$$

In the above equations, the partial correction factors \mathcal{C}_{ijl}^{ks} and $\mathcal{F}_{ik}^{s(p)}$ are introduced and defined in D. It is particularly shown that condensing Eq. (20) in Eq. (19a) and (19c) leads to the same corrected coefficient $\Lambda_{ik}^{(p)}$ which appears in both Eqs. (21a) and (21b).

The reduced order model defined by Eqs. (21) deserves attentions, since it involves *only* the bending modal coordinates $x_k(t)$ and the piezoelectric voltages $V^{(p)}$. If needed, the non bending modal coordinates $\eta_s(t)$ can be computed with Eq. (19b) and the whole spatio-temporal dynamics reconstructed by Eq. (10). A recent work [58] shows that the static condensation used in the present work is valid as long as the non bending modes natural frequencies are larger than 6 time the natural frequencies of the bending modes, $\omega_s > 6\omega_r$.

4.2. The modified STEP (M-STEP)

A direct procedure to obtain the condensed coefficients $(\Gamma_{ij}^k, \Lambda_{ik}^{(p)})$ would be to apply Eq. (22a,b) to the coefficients $a_{ij}^k, b_{ij}^k, \chi_k^{(p)}$ and $\Theta_{ik}^{(p)}$ computed with the classical STEP. However, it requires either to include all the modes in the basis, or to be able to identify the appropriated modes to accurately compute its nonlinear dynamic responses. The main drawback of this approach relies in its computational cost since many modes must be included for accuracy, as shown in Section 5.2 and in [49].

To overcome this issue, the modified STEP (M-STEP), introduced in [49], is used. It is worth noticing that the idea of this method was proposed earlier, [73], in the case of microsystems. If the STEP relies on the prescription of the modal displacements on all the degrees of freedom (dofs) of the finite element mesh (*i.e.* on the three components of the modal displacement fields prescribed on all the nodes), the principle of the M-STEP consists in prescribing only the transverse displacements on a particular set of nodes. The motions of the other dofs are therefore left free, such that their effect is implicitly taken into account, in particular the in-plane and thickness motions resulting from the effect of higher order modes.

In this framework, we now define the *master dofs* as the degrees of freedom with prescribed displacements and *slave dofs* the free ones, respectively denoted with indexes M and S , and such that the master dofs here consist of only transverse components. We now decompose the displacement \mathbf{U} and the internal force vectors \mathbf{f}^{int} as:

$$\mathbf{U} = \begin{bmatrix} \mathbf{U}_M \\ \mathbf{U}_S \end{bmatrix}, \quad \mathbf{f}^{\text{int}} = \begin{bmatrix} \mathbf{f}_M^{\text{int}} \\ \mathbf{f}_S^{\text{int}} \end{bmatrix}. \quad (23)$$

The M-STEP is illustrated by detailing the different steps to compute the ROM coefficients $(\Gamma_{ii}^k, \Lambda_{ii}^{(p)})$, with $i, k \in [1, \dots, N_B]$. The proposed method consists in prescribing:

$$\begin{cases} \mathbf{U}_M = \lambda \Phi_i^M, \\ \mathbf{f}_S^{\text{int}} = \mathbf{0}, \\ V^{(p)} = 0 \end{cases} \quad (24)$$

with $\lambda \in \mathbb{R}$ an amplitude factor of the mode Φ_j . Then, solving the static problem $\mathbf{f}^{\text{ext}} = \mathbf{f}^{\text{int}}(\mathbf{U})$ with the FE code leads to compute the internal force vector $\mathbf{f}_M^{\text{int}}(\mathbf{U})$ on the master nodes and the displacement \mathbf{U}_S on the slave nodes. In addition, the resulting charge $Q_{ii}^{(p)}$ is also computed with free slave dofs. The whole problem finally reads:

$$\mathbf{U} = \begin{bmatrix} \lambda \Phi_i^M \\ \mathbf{U}_S \end{bmatrix}, \quad \mathbf{f}^{\text{int}} = \mathbf{f}_e = \begin{bmatrix} \mathbf{f}_M^{\text{int}} \\ \mathbf{0} \end{bmatrix}, \quad (25)$$

$$Q_{ii}^{(p)} = - \left[\mathbf{f}_c^{(p)} + \frac{1}{2} \mathbf{P}_c^{(p)} \mathbf{U} \right]^T \mathbf{U} \quad \forall p \in [1, P].$$

To write the equivalent expressions in the modal space, we first assume that by letting free the membrane and thickness motions,

we have $\eta_s \neq 0$ and $F_s = 0$ for $s \in [N_B + 1, \dots, N]$, thus leading to consider that Eqs. (21) are valid. We assume also that the orthogonality property of the bending modes is still verified, that means $x_i \simeq \lambda$ and $x_j \simeq 0$ for $i, j \in [1, \dots, N_B]$, $i \neq j$. In Eqs. (25), multiplying the internal force vector and writing the electric charge with modal coordinates leads to:

$$\Phi_k \mathbf{f}^{\text{int}} = \delta_{ik} \omega_k^2 x_i + \Gamma_{iii}^k x_i^3 \quad (26a)$$

$$Q_{ii}^{(p)} = -\chi_i^{(p)} x_i - \frac{1}{2} \Lambda_{ii}^{(p)} x_i^2, \quad (26b)$$

where the coefficient $\chi_i^{(p)}$ are obtained with the procedure of Section 3.1. The condensed coefficients $(\Gamma_{iii}^k, \Lambda_{ii}^{(p)})$ can then be directly computed by prescribing modal displacements of the bending basis on a well chosen part of the structure. The procedure can be generalized for coefficients $\Gamma_{ijj}^k, \Gamma_{ijj}^k, \Gamma_{ijj}^k$ and $\Lambda_{ij}^{(p)}$, by prescribing $\mathbf{U}_M = \lambda_i \Phi_i^M \pm \lambda_j \Phi_j^M$ or $\mathbf{U}_M = \lambda_i \Phi_i^M \pm \lambda_j \Phi_j^M \pm \lambda_l \Phi_l^M$ like in the standard STEP [15]. The accuracy of this method has been shown for the computation of the Γ_{ijj}^k in the case of elastic structures [49]. In Sections 5 and 6, we will demonstrate its efficiency to compute the ROM coefficients $\Lambda_{ij}^{(p)}$.

4.3. Frequency responses

In the following sections, the frequency (periodic) response of the reduced order model will be computed by implementing Eq. (21a) in the continuation software Manlab. It combines the harmonic balance method (HBM) and asymptotic numerical method (ANM) [74], including also a stability analysis based on the Floquet theory and Hill method [75,76]. Eq. (21a) is rewritten in the state space and with a quadratic recast of the nonlinear terms, to improve the performance of the continuation procedure. The system will be forced by applying sine voltages $V^{(p)}(t) = V_0^{(p)} \sin(\Omega t)$, without mechanical excitation ($F_k = 0$). In this case Eq. (21a) is now written, for all $k = 1, \dots, N_B$:

$$\begin{cases} \dot{x}_k = v_k \\ \dot{v}_k = -\omega_k^2 x_k - 2\zeta_k \omega_k v_k - \sum_{p=1}^P \chi_k^{(p)} V_0^{(p)} P - \sum_{p=1}^P \sum_{i=1}^{N_B} \Lambda_{ik}^{(p)} x_i V_0^{(p)} P - \sum_{i=1}^{N_B} \sum_{j=1}^{N_B} \sum_{l=1}^{N_B} \Gamma_{ijl}^k S_{ij} x_l \\ 0 = S_{ij} - x_i x_j \\ 0 = \sin(\Omega t) - P. \end{cases} \quad (27)$$

The new unknowns contains the components of the system in the state space $x_1, x_2, \dots, x_{N_B}, v_1, v_2, \dots, v_{N_B}$ and some auxiliary variables $S_{11}, S_{12}, \dots, S_{N_B N_B}, P$ to obtain the quadratic form. A linear modal damping ζ_k is also added in the system.

The above described ANM-HBM will also be used to compute the backbone curve of a given mode k . It is obtained with the periodic solutions of (27) (of frequency ω) with no forcing ($P = 0$), with $\zeta_k = \lambda$ set as the bifurcation parameter (see [75] for details) and by initiating the continuation branch on $\omega = \omega_k$ with a very low modal amplitude. The backbone curve will also be plotted around the parametric resonance (see Figs. 4, 11, 14), which is located around $\omega = 2\omega_k$. For this, if the backbone curve around the main resonance is plotted with the points of coordinate (frequency, amplitude) = (ω, w) , the one around the parametric resonance is just the same data plotted with points of coordinates $(2\omega, w)$.

5. Validation test cases

In this section, two test cases are presented. They consist in piezoelectric symmetric beams, with geometries chosen such that they can be investigated with the analytical model of E. In the first example, a hinged-hinged beam with very thin piezoelectric

patches is discretized with a refined mesh to compare the ROM coefficients computed with the method of Sections 3 and 4.2 to analytical values. The advantage of the hinged-hinged boundary conditions is the simple form of the mode shapes, which allows to compute the nonlinear coefficients at hand and facilitates comparisons between analytical and numerical values. The second example consists of a clamped-clamped beam modelled with a coarse mesh, which aims first at analyzing the effect of the high order modes of the modal basis on the nonlinear dynamics of the low frequency bending modes, and secondly at obtaining reference computations with direct time simulations in a reasonable time. Besides, the nonlinear dynamics of an elastic clamped-clamped beam was extensively investigated in recent studies [15,49], and provides thus a convenient framework for the present paper, that focuses on the piezoelectric coupling. Numerical models are built with the finite element code Abaqus [39].

5.1. A hinged-hinged tri-layered beam

The first test case is a hinged-hinged bimorph with a rectangular cross-section and thin piezoelectric patches that cover the whole length of the beam, as depicted in Fig. 2. The length is $L = 1$ m, the width is $b = 20$ mm and the thicknesses of the elastic and piezoelectric layers are $h_e = 0.5$ mm and $h_p = 0.2$ mm, such that low aspect ratios and very thin patches are considered. A numerical model with a refined mesh is constructed and discretized with 3D quadratic 20-noded hexahedron elements in Abaqus (C3D20R elements for the elastic part and C3D20RE for the piezoelectric parts): 80 elements in length, 4 elements in width and 6 elements in the thickness (4 for the elastic part and 1 for each piezoelectric layer), for a total of 30999 dofs. The piezoelectric material is PIC151 [77]. The geometric and material constants of this test case are provided in Table 1.

Linear coupling coefficients $\chi_k^{(p)}$. The coefficients $\chi_k^{(p)}$ are computed following the procedure of Section 3.1. Table 2 gathers the values obtained with this method (labeled FE), as well as those stemming from the analytical model based on an Euler-Bernoulli kinematics presented in E. With this configuration, the coupling coefficients of the even bending modes are zero; it is due to the symmetry of the structure. Indeed, according to Eq. (E.10), the coupling coefficients $\chi_k^{(p)}$ are proportional to the difference of slope between the two ends of the piezoelectric patches, which is zero for the even modes. The first six lines of Table 2 show an excellent agreement between the analytical and numerical (FE) results, of about 0.5% for the short circuit natural frequencies f_k and less than 0.2% for the coupling coefficients $\chi_k^{(p)}$. Those results thus perfectly validate the computation procedure of Section 3.1.

To illustrate the efficiency of the procedure, the effective electro-mechanical coupling factors (EEMCF), which are more commonly used in the literature, are also computed. They are dimensionless and defined, for a given mode k , by [46]¹:

$$k_{\text{eff},k}^{(p)} = \sqrt{\frac{\hat{\omega}_k^{(p)2} - \omega_k^2}{\omega_k^2}}, \quad (28)$$

where $\hat{\omega}_k^{(p)}$ denotes the natural frequency of the k^{th} mode with open-circuited electrodes at the p^{th} piezoelectric patch. With the finite element code, the $\hat{\omega}_k^{(p)}$ are computed with a standard modal analysis, for which a reference potential (typically $\psi = 0$) is prescribed at all the nodes of one electrode of the p -th. patch and an equipotentiality condition is imposed for the nodes of the other electrode, the value of the potential being left free. In practice, a

multipoint constraint is prescribed in the FE code, in the form of a linear constraint equation between the electric potential degrees of freedom of the electrode. As explained in [41], we define the coupling coefficient associated to $k_{\text{eff},k}^{(p)}$ by:

$$\chi_{\text{eff},k}^{(p)} = k_{\text{eff},k}^{(p)} \omega_k \sqrt{C^{(p)}}, \quad (29)$$

in order to compare its value to $\chi_k^{(p)}$. In the case of a single degree of freedom (one mode) system, $\chi_{\text{eff},k}^{(p)}$ and $\chi_k^{(p)}$ would be strictly equal, as shown in [41]. However, in the present case of a multi-mode structure, the other modes than the k -th influence the value of the open circuit natural frequency $\hat{\omega}^{(p)}$ and make a difference between $\chi_k^{(p)}$ and $\chi_{\text{eff},k}^{(p)}$. This is observed by comparing the last two rows of Table 2, which highlights a significant error ($> 10\%$). Comparable discrepancies were found in [79], where authors propose to correct the coupling coefficient by taking into account other modes in the basis. These discrepancies between $\chi_{\text{eff},k}^{(p)}$ and $\chi_k^{(p)}$ shows that our method has to be preferred to accurately compute the value of the linear piezoelectric coefficients $\chi_k^{(p)}$ of our ROM. It is in particular more accurate than the one consisting in computing the EEMCF $k_{\text{eff},k}$ (by two modal analyses, one in short circuit, one in open circuit and Eqs. (28) & (29)), and computationally more efficient, since only one modal analysis is required.

Nonlinear coefficient Γ_{ijl}^k . The cubic nonlinear coefficients Γ_{ijl}^k are computed using the M-STEP of Section 4.2. The results, for some values of $(i, j, l; k)$ associated to the first three bending modes, are compared in Table 3 to those obtained with the analytical model of E. The agreement is excellent. It firstly shows that the deformation of the present laminated structure is close to an Euler-Bernoulli kinematics. Secondly, it validates once more the M-STEP, in accordance with the results reported for an homogeneous clamped beam in [49]. To once more illustrate the necessity of including the non bending modes in the ROM, Table 3 also includes the values of the cubic coefficients b_{ijl}^k associated to the same bending modes $(i, j, l; k)$. The comparison with the Γ_{ijl}^k presents very large discrepancies, showing again the importance of the correction in Eq. (22a). The STEP and the M-STEP were applied by prescribing modal displacements of respectively $\max(\lambda_i \Phi_i) = h/20$ and $\max(\lambda_i \Phi_i) = h/2$ on the structure, in accordance with the results of [15,49].

Parametric coefficients $\Lambda_{ij}^{(p)}$. In the same manner than for the cubic coefficients Γ_{ijl}^k , the parametric coefficients $\Lambda_{ij}^{(p)}$ are computed with the M-STEP described in Section 4.2. In Table 4, they are compared to analytical values (from the model of E) and to coefficients $\Theta_{ij}^{(p)}$ computed with the standard STEP of Section 3.2. According to Eq. (E.10), the linear coupling coefficients of axial modes $\chi_s^{(p)}$ vanish with this configuration. It is due to the boundary conditions and because the piezoelectric patches cover the whole length of the beam. Therefore, considering the expression of the correction factor $\mathcal{F}_{ik}^{s(p)}$ in Eq. (22b), one concludes that the correction of $\Theta_{ij}^{(p)}$ to obtain the condensed coefficient $\Lambda_{ij}^{(p)}$ is only brought by couplings to thickness modes and not to axial modes. Another property of the parametric coefficients with this structure is that $\Lambda_{ij}^{(p)} = 0$ if $i \neq j$, according to Eq. (E.10) and because the bending mode shapes of a hinged-hinged beam are sine functions. Thus, only coefficients $\Lambda_{ii}^{(up)}$ are presented in Table 4.

As for the cubic coefficient Γ_{ijl}^k , large discrepancies are reported between coefficients $\Lambda_{ij}^{(p)}$ and $\Theta_{ij}^{(p)}$, because of the correction brought by the NB modes in Eq. (22b). We checked that those modes are thickness modes only, as predicted by the analytical

¹ In [46], the denominator of $k_{\text{eff},k}^{(p)}$ is in fact the open circuit natural frequency $\hat{\omega}_k^{(p)}$

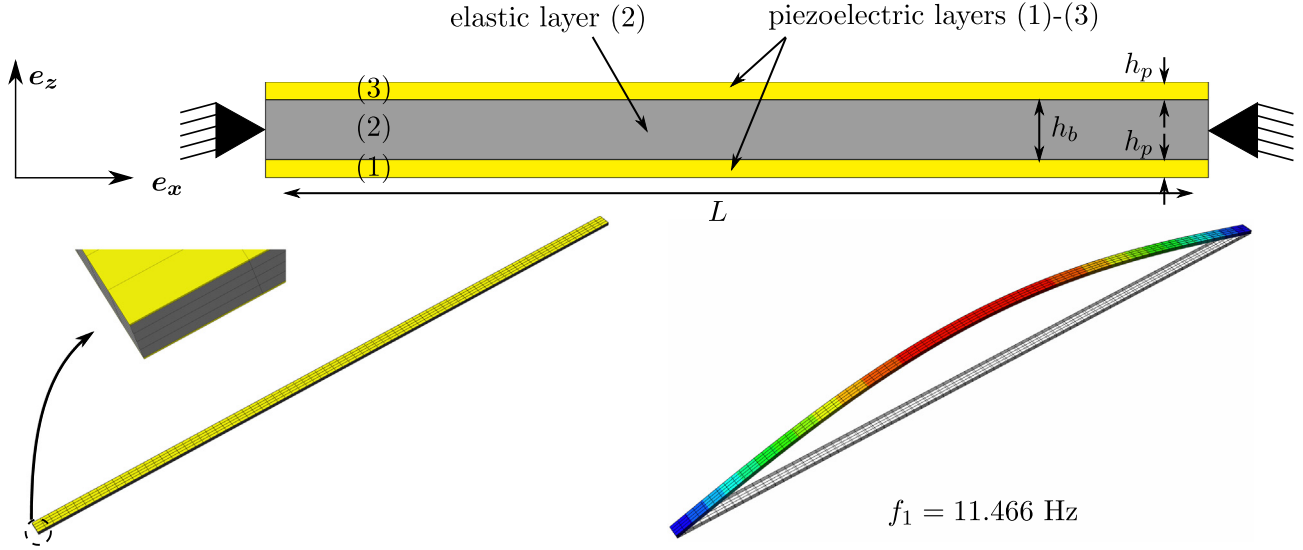


Fig. 2. Geometry of the hinged-hinged bimorph (up). Mesh and first eigenmodes computed by the finite element code (down).

Table 1

Material parameters of the model in the FE code. The characteristics of PIC 151 are taken from [78]. Note that the piezoelectric coefficients d_{ikl} instead of the coefficients e_{ikl} of Eq. (3) are prescribed here. ($e_{mij} = d_{mkl}c_{kij}^E$).

		Elastic core (Titanium)	Piezoelectric patches (PIC151)
Densities	kg/m ³	4500	7760
Young's modulus	GPa	72	-
Poisson's ratio	-	0.34	-
Stiffness constants	GPa	-	$c_{1111}^E = c_{2222}^E$ 107.6
		-	c_{3333}^E 100.4
		-	c_{1122}^E 63.12
		-	$c_{1133}^E = c_{2233}^E$ 63.85
		-	$c_{1313}^E = c_{2323}^E$ 19.62
		-	c_{1212}^E 22.24
Piezoelectric constants	m/V	-	$d_{311} = d_{322}$ -2.14×10^{-10}
		-	d_{333} 4.23×10^{-10}
		-	$d_{113} = d_{123}$ 6.10×10^{-10}
Dielectric constants	nF/m	-	$\epsilon_{33}^E = \epsilon_{22}^E$ 9.83
		-	ϵ_{33}^E 7.54

Table 2

Frequencies and linear coupling coefficients on the upper electrode $\chi_k^{(up)}$ for the hinged-hinged beam of Fig. 2. The modes considered in the index k range from the first to the fifth bending eigenmodes. On the lower electrode the coefficients verify $\chi_k^{(down)} = -\chi_k^{(up)}$.

Bending modes		$k = 1$	$k = 2$	$k = 3$	$k = 4$	$k = 5$	$k = 6$
f_k , analytical	[Hz]	11.399	45.595	102.59	182.38	284.97	410.35
f_k , FE	[Hz]	11.466	45.858	103.16	183.36	286.39	412.28
Error on f_k	[%]	0.41	0.52	0.56	0.56	0.50	0.47
$\chi_k^{(up)}$, analytical	[N V ⁻¹ kg ^{-1/2}]	5.8212×10^{-3}	0	1.7464×10^{-2}	0	2.9105×10^{-2}	0
$\chi_k^{(up)}$, FE	[N V ⁻¹ kg ^{-1/2}]	5.8106×10^{-3}	0	1.7434×10^{-2}	0	2.9066×10^{-2}	0
Error on $\chi_k^{(up)}$	[%]	0.18		0.17		0.13	
$\chi_{k,eff}^{(up)}$, FE	[N V ⁻¹ kg ^{-1/2}]	5.2776×10^{-3}	0	1.5818×10^{-2}	0	2.6388×10^{-2}	0
Error on $\chi_{k,eff}^{(up)}$	[%]	10.6		14.2		10.3	

model. One can note that the signs of $\Lambda_{ij}^{(p)}$ and $\Theta_{ij}^{(p)}$ are different, showing again the importance of including the NB modes in the ROM. On the contrary, the values of $\Lambda_{ij}^{(p)}$ obtained with the M-STEP are in good agreement with analytical ones, thus validating our numerical procedure. A systematic error of the order of 5% must be noted, probably due to the Euler–Bernoulli kinematics constraints of the analytical model, which are left free in the FE computations since they rely on 3D finite elements.

The sensitivity of the computations to the modal amplitude factor λ with the M-STEP was also investigated. The results in Fig. 3 highlight a range of validity centered around $\max(\lambda_i \Phi_i) = h/2$, which is similar to the sensitivity observed in the case of the cubic coefficients Γ_{ijt}^k of a clamped beam [49].

Frequency response. The periodic frequency response of the bimorph was computed around its first resonance with Manlab, as explained in Section 4.3. To ensure both a direct and a parametric driving of the structure, only one of the patches (the

Table 3

Nonlinear coefficients Γ_{ij}^k and b_{ij}^k , in $[\text{N m}^{-3}\text{kg}^{-2}]$, computed analytically, with the M-STEP and the STEP, and relative errors, for the hinged-hinged beam of Fig. 2. All the results were obtained by computing the static responses with $\max(\lambda\Phi_i) = h/2$.

Bending modes (i, j, l, k)	(1, 1, 1; 1)	(2, 2, 2; 2)	(3, 3, 3; 3)	(1, 1, 2; 1)	(1, 2, 2; 1)
Γ_{ij}^k , analytical	2.2057×10^9	3.5291×10^{10}	1.7866×10^{11}	0	8.8227×10^9
Γ_{ij}^k , M-STEP	2.1991×10^9	3.5166×10^{10}	1.7783×10^{10}	7.50×10^2	8.8830×10^9
Error [%]	0.30	0.36	0.46		0.68
b_{ij}^k , STEP	1.5076×10^{10}	2.4109×10^{11}	1.2194×10^{12}	1.31×10^6	1.2056×10^{11}
Error [%]	584	583	583		1266

Table 4

Parametric coefficients $\Lambda_{kk}^{(up)}$ and $\Theta_{kk}^{(up)}$, in $[\text{N m}^{-1}\text{V}^{-1}\text{kg}^{-1}]$, computed analytically, with the M-STEP and the STEP, and relative errors, for the hinged-hinged beam of Fig. 2. These coefficients are identical on the two electrodes ($\Lambda_{kk}^{(up)} = \Lambda_{kk}^{(down)}$). All the results were obtained by computing the static responses with $\max(\lambda\Phi_i) = h/2$

Bending modes	$k = 1$	$k = 2$	$k = 3$	$k = 4$	$k = 5$
$\Lambda_{kk}^{(up)}$, analytical	-3.475	-13.90	-31.28	-55.60	-86.88
$\Lambda_{kk}^{(up)}$, M-STEP	-3.289	-13.14	-29.48	-52.57	-82.59
Error [%]	5.7	5.7	6.1	5.8	5.2
$\Theta_{kk}^{(up)}$, STEP	4.783	27.71	60.19	85.17	85.43
Error [%]	238	300	292	253	202

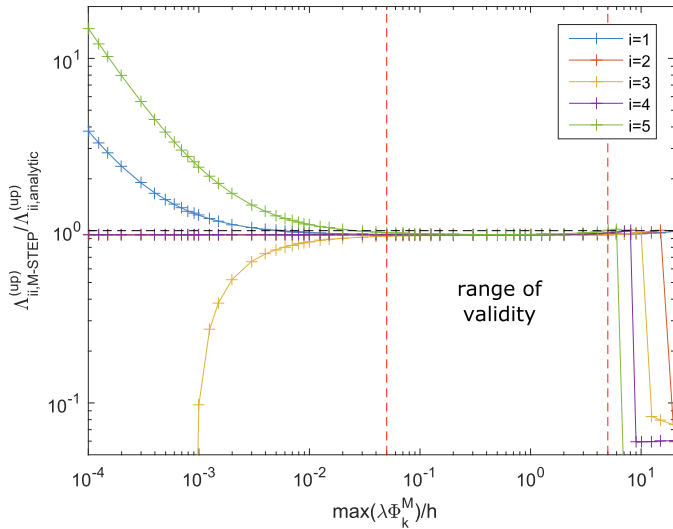


Fig. 3. Dependence of the parametric coefficient $\Lambda_{ii}^{(up)}$ with regard to the prescribed displacement amplitude for different modes $i = 1, 2, 3, 4, 5$, computed by the M-STEP. Black dashed line: reference analytical value ($\Lambda_{ii}^{(up),FE} = \Lambda_{ii}^{(up),AN}$). Red dashed lines: limits of the range of validity. (For interpretation of the references to colour in this figure legend, the reader is referred to the web version of this article.)

upper one) was driven ($V^{(up)} = V_0$ and $V^{(down)} = 0$), to obtain both an axial and a bending actuation. A high actuation amplitude $V_0 = 150$ V was chosen, to reach the parametric instability. The dynamic responses were computed with a damping $\xi_k = 2\%$, identical for all the oscillators of the basis. The system (27) was solved by increasing the number N_b of bending modes, and no significant difference was observed in the dynamic response. The results shown in Fig. 4 thus present the resonance curves with direct and parametric excitation with only one mode in the basis ($N_b = 1$). The parametric response was obtained, after period doubling bifurcations, by forcing the system in the neighbourhood of twice the natural frequency of the first mode ($\Omega \simeq 2\omega_1$). One can observe that in the present case, the amplitude at resonance is larger with direct excitation than that with parametric excitation. Fig. 4 also shows the backbone curve of the first mode. As expected, both forced responses are articulated around this backbone curve.

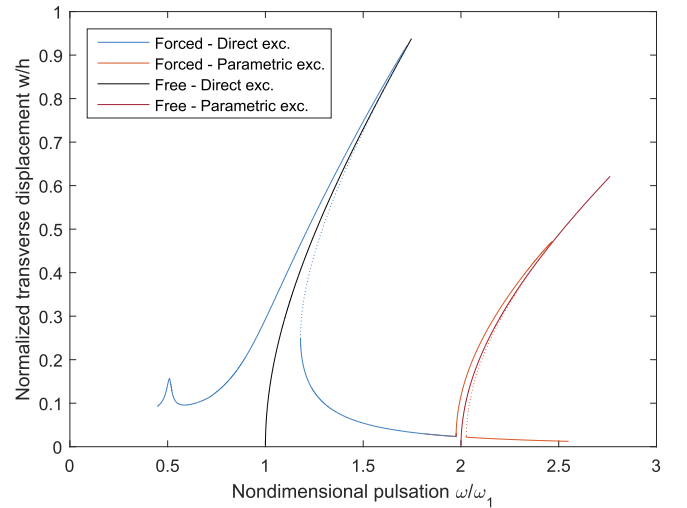


Fig. 4. Nonlinear free and forced responses of the hinged-hinged beam to the voltage signal $V = V_0 \sin(\Omega t)$ with $V_0 = 150$ V applied on the upper patch, computed with Manlab, with one mode in the ROM and 10 harmonics in the HBM. The maximum transverse displacement w over a period, at the center of the beam, normalized by the beam thickness $h = h_b + 2h_p$, is shown.

5.2. A clamped-clamped tri-layer beam

In order to deeply understand the coupling of the low frequency bending modes with the high frequency NB (thickness/ axial) modes, we investigate a test case (see Fig. 5) with a coarse FE mesh. It allows to compute all the modes of the structure in order to condense all the NB modes with Eq. (22). The beam is symmetrical in both transverse and axial directions, with two piezoelectric patches of equal thickness h_p located in the central part of the beam. Their length $L_p = x_+ - x_-$ was chosen lower than the total length L of the beam to ensure a linear piezoelectric coupling with the bending modes (the mode shapes must have a non zero slope at the ends of the piezoelectric patch, see Eq. (E.10)). To compare our results to the analytical model of E, we set the same elastic constants to all the parts of the beam (the ones of PIC151 of the second column of Table 1), the only material difference being in the piezoelectric constants e_{kij} , set to zero in the elastic parts. In the computations, the lengths are $L = 1\text{m}$, $L_p = 600\text{mm}$, the cross

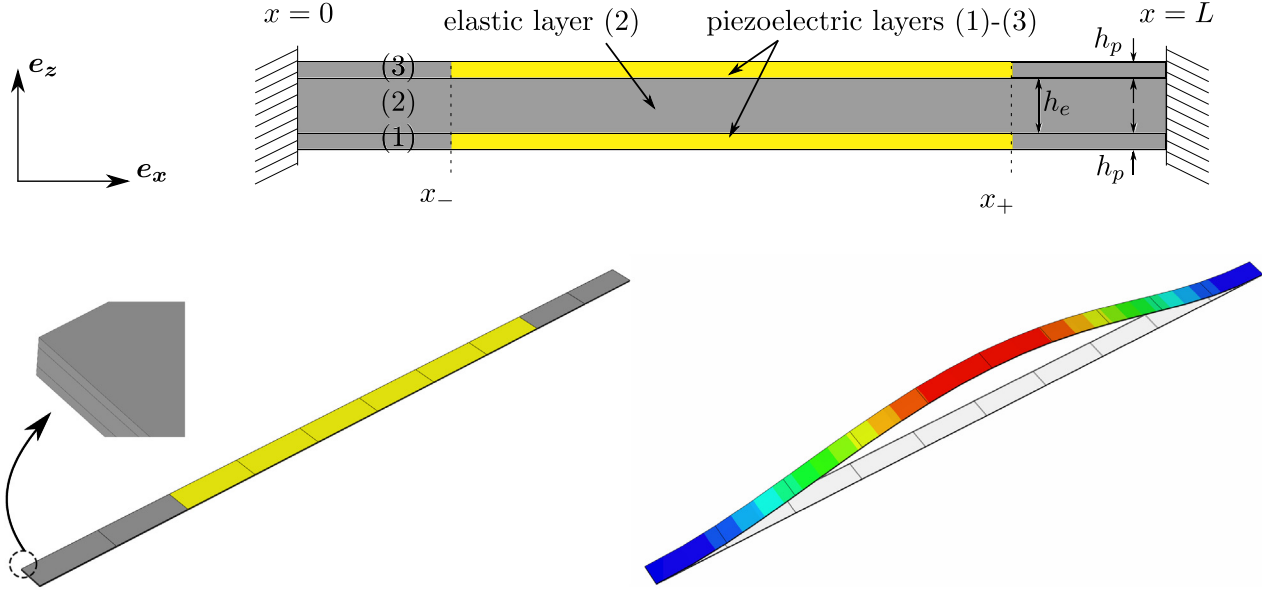


Fig. 5. Geometry of the bi-clamped piezoelectric beam (up). Mesh and first eigenmode computed by the finite element code (down).

section is rectangular of width $b = 20$ mm, the thicknesses are $h_e = 1$ mm and $h_p = 0.5$ mm, so that a low aspect ratio is obtained ($(h_e + 2h_p)/L = 2 \times 10^{-3}$). The mesh is made of 20-noded hexahedron elements, and consists of ten elements in length, one element in the width and one element for each layer in the thickness. The full model has 30 elements and 726 free degrees of freedom. This coarse mesh allowed us to compute all the 726 eigenmodes of the system as well as its dynamic response in the steady state, by standard time integration, in a reasonable computational time.

Static condensation. We first investigate the convergence of the computation of the parametric coefficient $\Lambda_{ij}^{(p)}$ with the condensation procedure of Section 4, namely with Eq. (22b). For this, the coefficients $\chi_s^{(p)}$ and a_{ik}^s are computed with the STEP for all the non bending modes of the modal basis ($s = N_B, \dots, N$) and used in Eq. (22b) to correct coefficient $\Theta_{11}^{(1)}$ to obtain $\Lambda_{11}^{(1)}$.

Fig. 6 confirms that the condensation has a huge effect on the values of $\Lambda_{11}^{(1)}$. Indeed, Fig. 6 (left) shows that it changes sign by progressively taking into account the NB modes in the basis. Fig. 6 (right) shows the frequency responses under parametric excitation, computed with one mode and different values of $\Lambda_{11}^{(up)}$: the amplitude of the response is small for a low number of modes in the basis (the resonance is even not observable for 1 to 4 non bending modes retained in the basis). It corresponds to very small values of $\Lambda_{11}^{(1)}$, achieved when the coefficient changes of sign. Then, increasing the number of non bending modes retained in the basis enable a slow convergence toward the converged parametric response of the system. This slow convergence is also illustrated in Figs. 8 and 7, that show the evolution of the correction factors $\mathcal{C}_{111}^{1s}/\Gamma_{111}^1$ and $\mathcal{F}_{11}^{s(up)}/\Lambda_{11}^1$ of Eqs. (22a,b) as a function of the non bending modes number. Results analogous to those shown in [49] are obtained here for the cubic coefficient Γ_{111}^1 convergence, as well as for the parametric coefficient Λ_{11}^1 convergence: one has to include a huge number of non bending modes, located in the high part of the spectrum, to achieve convergence. This slow convergence is addressed in deep in [49] to which the interested reader can refer for details.

An interesting result is that this convergence appears slower for $\Lambda_{11}^{(up)}$ than for Γ_{111}^1 : looking in deep at Figs. 8 and 7, one observe that

25 modes are necessary to have $\mathcal{F}_{11}^{s(up)}/\Lambda_{11}^{(up)} < 1\%$ whereas only 15 modes are sufficient to have $\mathcal{C}_{111}^{s(up)}/\Gamma_{111}^1 < 1\%$. To further illustrate this slow convergence, Table 5 presents the mode shapes of the ten modes with the higher values of $\mathcal{F}_{11}^{s(up)}/\Lambda_{11}^1$, i.e. that bring the highest correction to Λ_{11}^1 . In the same manner than what presented in [49] for the convergence of the cubic elastic coefficients Γ_{ijl}^k , the more significant modes are thickness modes (that present predominantly a transverse through the thickness motion). In particular, only one axial mode (the fourth one) appears in this Table.

The M-STEP is finally applied on the structure to compute the coefficients Γ_{111}^1 and $\Lambda_{ii}^{(up)}$. Since the structure is only meshed with one element in the thickness of the elastic part and of the whole width of the beam, only a few nodes are placed in the middle line. We thus applied the M-STEP on the plane $y = 0$, that means in the middle plane in the width, such that the M-STEP involves a sufficient number of master nodes. The results are gathered in Table 6. The relative error with the analytical values shows an excellent agreement: the small error found for the $\Lambda_{ii}^{(up)}$ can be explained by the coarse mesh or/ and by the validity of the assumptions of the analytical model. The converged values of the $\Lambda_{ii}^{(up)}$ obtained by the condensation procedure explained above are also mentioned in Table 6, with a significant error of unknown origin.

Frequency response. The direct and parametric frequency responses of the clamped-clamped bimorph were computed around its first resonance with both Manlab, as explained in Section 4.3, and direct integration in Abaqus. For the latter, the implicit Newmark average acceleration method was used (with parameters $\alpha = 0, \beta = 1/4$ and $\gamma = 1/2$). The fixed time increment was $\Delta t = 0.01$ s. To compute a frequency response curve, a discrete number of driving frequency increments was chosen. For each one, the time response was computed until the steady state. To reach the upper branch of the resonance, the initial conditions for a time integration of a given frequency increment were chosen as the final state of the system at the previous frequency increment, to minimize the effects of the transient and remain in the basin of attraction of the branch. The maximum amplitude in the steady state gives one point on the resonance curve. The duration of each computation step was also chosen as an integer multiple of the period of the excitation, in order to have a continuous driving signal from

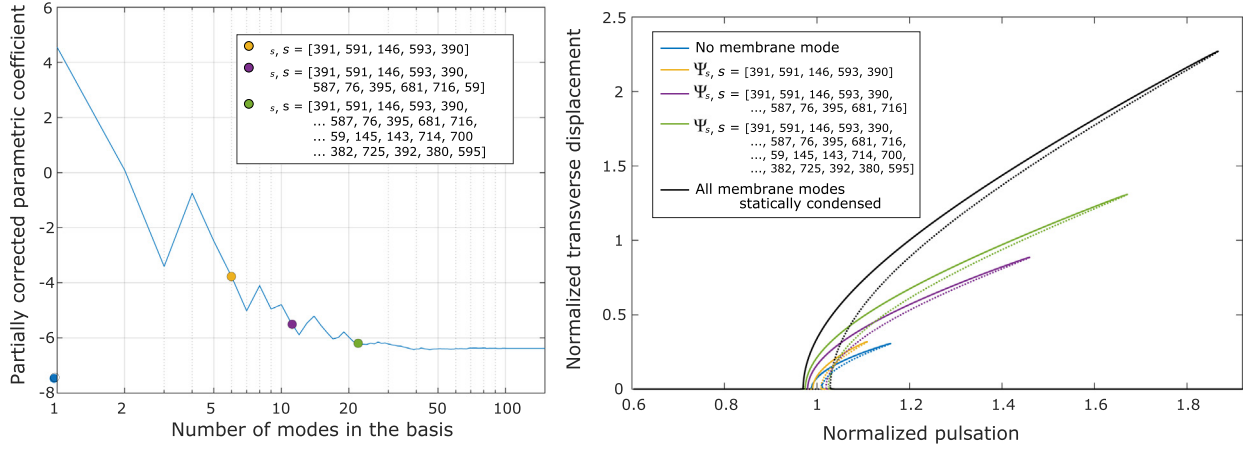


Fig. 6. (left) Value of Λ_{11}^1 [$\text{N m}^{-1}\text{V}^{-1}\text{kg}^{-1}$] as a function of the number of retained NB modes in Eq. (22b), for the clamped–clamped beam of Fig. 5. (right) First parametric resonance, for which the maximum transverse displacement w over a period, at the center of the beam, normalized by the beam thickness $h = h_b + 2h_p$, is shown as a function of $\Omega/(2\omega_1)$. For this simulation, only the first mode is kept in the ROM (which reduces to a single Mathieu–Duffing oscillator), with $\xi_1 = 2\%$, 20 harmonics in the HBM and a pure parametric driving is set, $V^{(\text{up})} = V^{(\text{down})} = V_p \sin \Omega t$ with $V_p = 15\text{V}$.

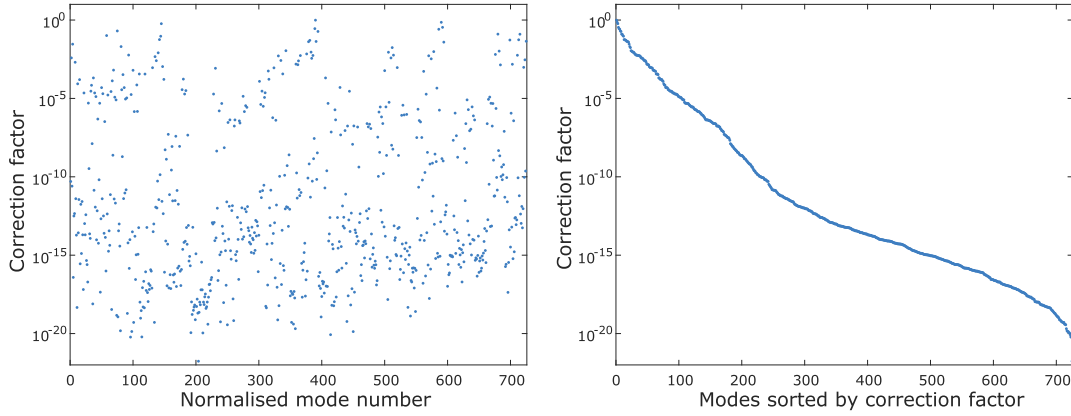


Fig. 8. Nondimensional correction factor $\mathcal{F}_{11}^{s(\text{up})}/\Lambda_{11}^1$ of all the NB modes for the clamped–clamped beam of Fig. 5, sorted with the NB mode number s (left) and by decreasing correction factor (right).

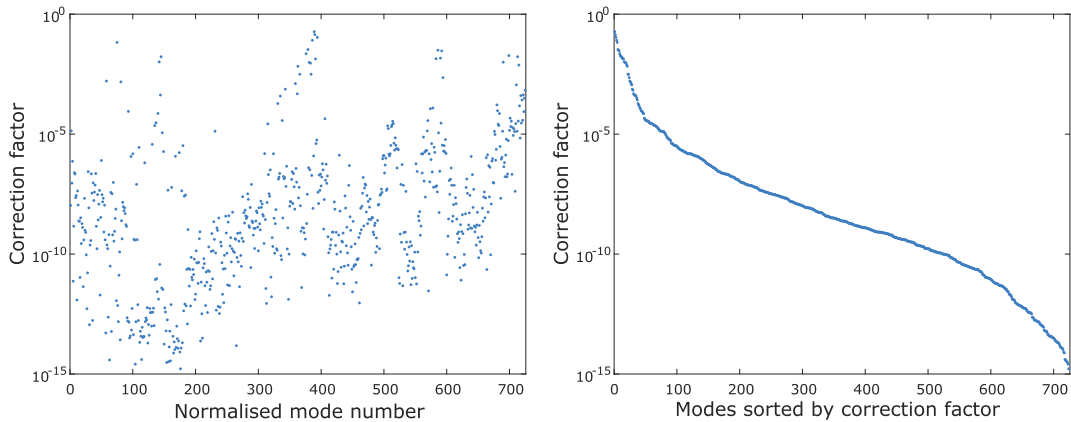


Fig. 7. Nondimensional correction factor $\mathcal{G}_{111}^{1s}/\Gamma_{111}^1$ of all the NB modes for the clamped–clamped beam of Fig. 5, sorted with the NB mode number s (left) and by decreasing correction factor (right).

one frequency increment to the other. 60 periods (resp. 120 for the parametric regime) were sufficient to reach the steady state. A viscous damping matrix \mathbf{D} proportional to the mass matrix was added

to the model, chosen such that $\mathbf{D} = \alpha \mathbf{M}$ with $\alpha = 2\xi\omega_1$ and $\xi = 2\%$. In the Manlab simulations, an equivalent modal damping was prescribed, such that $\zeta_k = \xi\omega_1/\omega_k$.

Table 5

Order of appearance in the basis (#), eigenfrequencies, correction factors $\mathcal{F}_{11}^{s(\text{up})}/\Lambda_{11}^1$ and shapes of the most relevant NB modes coupled with the first bending mode of the clamped-clamped beam of Fig. 5. The colors scale the modulus of the displacement field, the green color denoting zero displacement, and arrows display the axial displacement for axial mode 76.

#	$\omega_l/(2\pi)$ [Hz]	$\mathcal{F}_{11}^{1(\text{up})}/\Lambda_{11}^1$	Shape	Section
391	8.704×10^5	-6.981×10^{-1}		
591	3.039×10^6	-5.483×10^{-1}		
146	5.405×10^4	4.168×10^{-1}		
593	3.039×10^6	-2.727×10^{-1}		
390	8.685×10^5	-2.019×10^{-1}		
587	3.030×10^6	-1.943×10^{-1}		
76	5.547×10^3	1.435×10^{-1}		
395	8.707×10^5	-1.335×10^{-1}		
681	3.963×10^6	2.531×10^{-1}		
716	8.127×10^6	-9.850×10^{-2}		

Table 6

Nonlinear coefficient Γ_{111}^1 , in $[\text{N m}^{-3}\text{kg}^{-2}]$, and parametric coefficient $\Lambda_{ii}^{(\text{up})}$, in $[\text{N m}^{-1}\text{V}^{-1}\text{kg}^{-1}]$, computed analytically, with the M-STEP and relative errors, for the clamped-clamped beam of Fig. 5. The coefficients are identical for both piezoelectric layers ($\Lambda_{ii}^{(\text{up})} = \Lambda_{ii}^{(\text{down})}$).

	Γ_{111}^1	$\Lambda_{11}^{(\text{up})}$	$\Lambda_{22}^{(\text{up})}$	$\Lambda_{33}^{(\text{up})}$	$\Lambda_{13}^{(\text{up})}$
Analytical value	1.2448×10^9	-6.0487	-22.6410	-48.6275	4.7842
Static condensation	1.2074e9	-6.3833	-26.4082	-54.8432	5.9974
Relative error [%]	3.1	5.6	16.7	12.8	25.4
M-STEP	1.2898×10^9	-6.2341	-23.2398	-49.5988	5.0075
Relative error [%]	3.6	3.1	2.6	2.0	4.6

For these computations, the same electric potential was set on the inner electrodes of the beam, whereas sine potentials were prescribed to the outer electrodes. Because of the chosen polarization of the patches, $\chi_k^{(\text{up})} = -\chi_k^{(\text{down})}$ and $\Lambda_{kk}^{(\text{up})} = \Lambda_{kk}^{(\text{down})}$ for the odd bending modes. Then, to obtain a bending (direct) excitation of the

beam, we prescribed opposite voltages in the upper and lower electrodes (*i.e.* $V^{(\text{up})} = -V^{(\text{down})} = V_d \sin(\Omega t)$) and a frequency $\Omega \simeq \omega_1$ close to the first natural frequency of the beam. On the contrary, for the parametric excitation, we chose the same voltages (*i.e.* $V^{(\text{up})} = V^{(\text{down})} = V_p \sin(\Omega t)$) and a driving frequency $\Omega \simeq 2\omega_1$

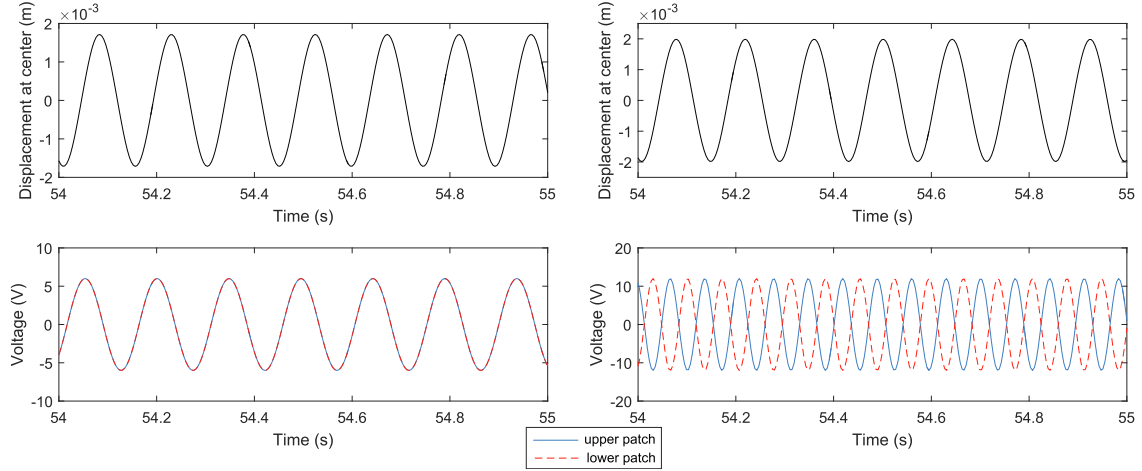


Fig. 9. Time signals of the displacements and outer electrode potentials, for the clamped–clamped beam of Fig. 5, in the steady state, computed with time integration in Abaqus, in the case of the direct (left) and parametric excitation (right).

twice larger than the first natural frequency. As depicted in Fig. 9, the electric potential signals on the upper and lower electrodes are in phase in the case of the direct excitation and out of phase for the parametric excitation. Moreover, in the case of the parametric driving at 2Ω , the response of the structure is subharmonic, at Ω .

We first check the modal convergence, in term of bending modes in (27), of the parametric resonance curve. As shown in Fig. 10, obtained with $V_p = 12V$, including the third mode in the basis leads to a significant change, which mainly consists of a decrease of the maximum of amplitude, whereas no substantial change of curvature is observed. We checked that including more bending modes was not necessary at this level of excitation. As a consequence, the ROM of Eqs. (27) with only $N_b = 2$ bending modes (the first and the third) seems an efficient ROM for the parametric response. Then, we compared the results of our ROM to the results of the direct time-integration with Abaqus. Fig. 11 shows the result: a perfect agreement is noticeable for both direct and parametric driving (we chose $V_d = 6V$ and $V_p = 12V$ for those computations). The free responses (backbone curves) are also shown. As expected, both parametric and direct responses are articulated around. The backbone curve makes appear a tongue which corresponds to a 1:5 internal resonance with the third mode, which was not observable on the forced responses due to the damping. For details about the internal resonance tongues, see e.g. [15].

6. Dynamic response computation of a realistic structure

The previous section aimed at computing the dynamic response of two ideal test cases, in order to provide a numerical validation of the methodology. In this section, we apply the same approach to a more realistic structure: a clamped–clamped bimorph, shown in Fig. 12. It is composed of an elastic central layer of length L_b , width b_b and thickness h_b and two piezoelectric patches of length L_p , width b_p and thickness h_p , glued at an axial location defined by x_- . The width of the patches is chosen smaller than that of the beam, $b_p < b_b$. For the computations, we chose $L = 90$ mm, $L_p = 45$ mm, $x_- = 5$ mm, $b_e = 13$ mm, $b_p = 10$ mm and $h_e = h_p = 0.5$ mm. The elastic and piezoelectric materials are respectively steel (of density $\rho_e = 7800$ kg/m³, Young’s modulus $Y_e = 210$ GPa and Poisson’s ratio $\nu_e = 0.38$) and PIC151 (with parameters of Table 1).

Since the structure is materially and geometrically symmetrical in the transverse direction, we use the condensed ROM of Eqs. (21a,b) to compute the nonlinear dynamics. For the computation

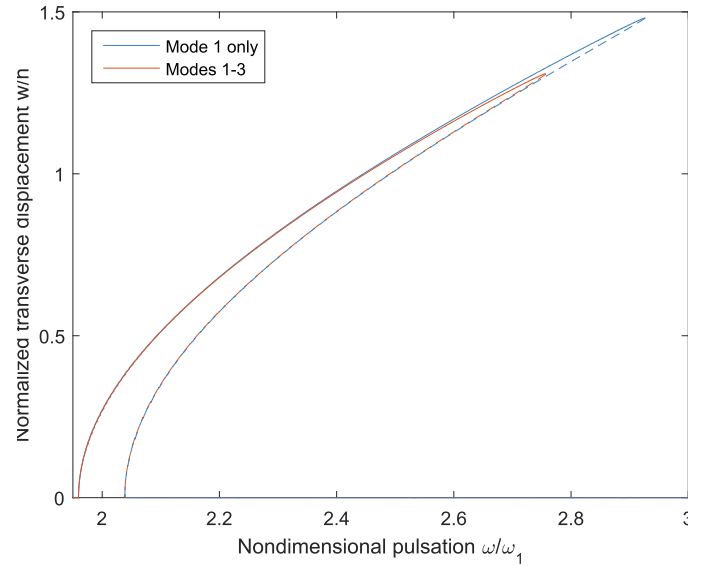


Fig. 10. Frequency response of the clamped–clamped beam of Fig. 5 at its first resonance with parametric excitation, computed with Matlab, with the first mode only and with the first and third modes in the ROM and 10 harmonics in the HBM. The maximum transverse displacement w over a period, at the center of the beam, normalized by the beam thickness $h = h_b + 2h_p$, is shown.

of the ROM coefficients, a standard modal analysis with short circuited electrodes enables to compute the bending modes (ω_k, Φ_k) (In practice, they can be identified manually or the axial displacement of all the nodes of the middle surface can be set to zero). Then, the procedure of Section 3.1 is used to compute the linear piezoelectric coefficients $\chi_k^{(p)}$, whereas the M-STEP is applied to compute the nonlinear coefficients Γ_{ijl}^k and $\Lambda_{ik}^{(p)}$. The maxima of the prescribed modal displacements were $\max(\lambda_k \phi_k) = h/2$ for the M-STEP, for any bending modes k .

Table 7 shows the numerical values of the natural frequencies $f_k = \omega_k/(2\pi)$ and the piezoelectric coefficients $\chi_k^{(p)}$. We also mention in the table the values of $\chi_k^{(p)}$ obtained with the EEMCF computation (using Eqs. (28) and (29) and two modal analyses, in short and open circuit). It shows again (see Section 5.1) that this later computation leads to significant errors, larger than 5%. Then, Table 8 gathers the values of the nonlinear coefficients Γ_{ijl}^k and $\Lambda_{ik}^{(p)}$ computed with the M-STEP. Conversely to the examples of

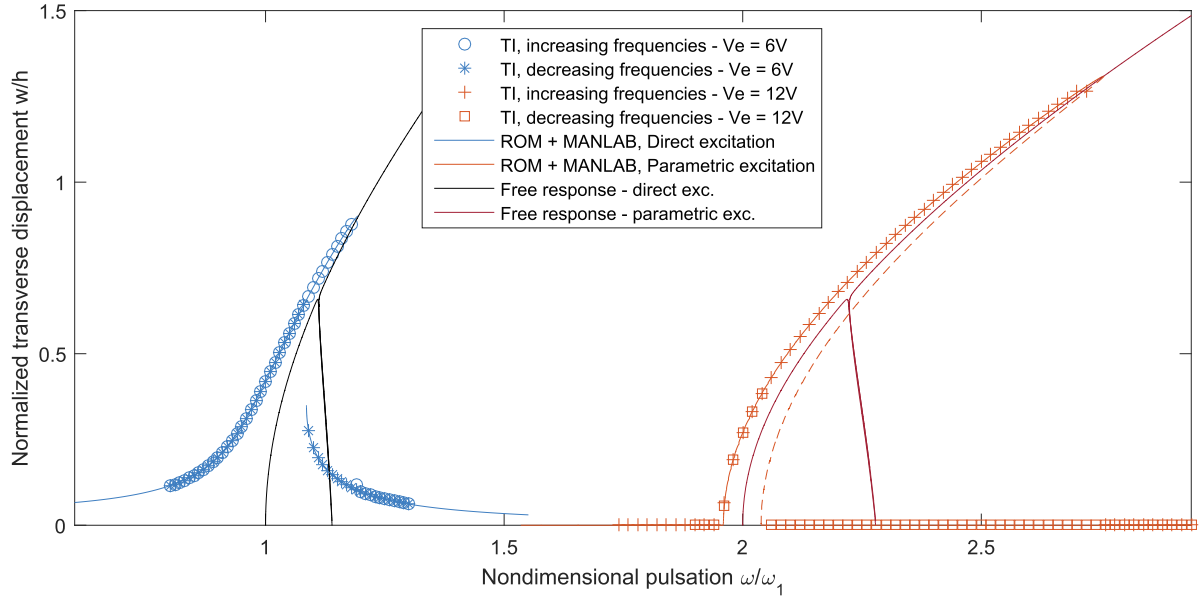


Fig. 11. Frequency response of the clamped–clamped beam of Fig. 5, driven by pure direct excitation around its first bending resonance ($\Omega \simeq \omega_1, V_d = 6 \text{ V}$) and with pure parametric excitation ($\Omega \simeq 2\omega_1, V_p = 12 \text{ V}$). Results from Manlab, with the first three bending modes in the ROM and 10 harmonics in the HBM, and by using time integration (TI) in Abaqus. The maximum transverse displacement w over a period, at the center of the beam, normalized by the beam thickness $h = h_b + 2h_p$, is shown.

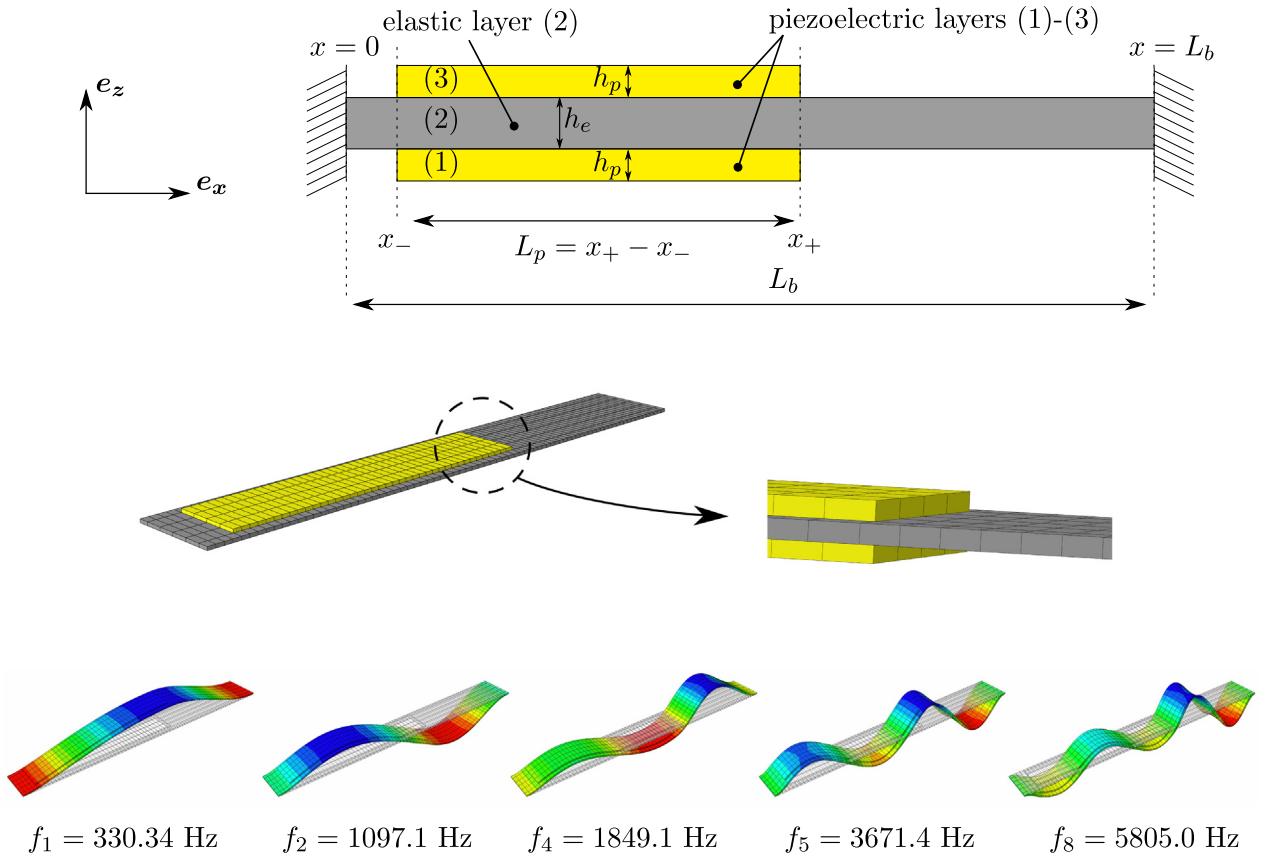


Fig. 12. Geometry of the straight piezoelectric beam (top), detail of the mesh (middle) and first bending modes (bottom) computed with the finite element code.

Section 5, all the coefficients are non-zero in the present case because of the dissymetry of the structure in the axial directions, clearly seen on the mode shapes in Fig. 12.

The convergence of the dynamical responses with the number of bending modes in the basis is now investigated with Manlab,

as explained in Section 4.3. For this, the free and parametric responses of the system are computed around its first resonance with different bases, including one, two, three and five bending modes. The results are depicted in Fig. 13. The comparison of the free responses show that a single mode is sufficient to predict

Table 7

Natural frequencies and linear coupling coefficients on the upper electrode of the realistic bimorph of Fig. 12, for the first six bending modes ($k = 1, \dots, 6$). $f_{k,FE}$ were computed with a modal analysis with short-circuited electrodes, $\gamma_{k,FE}^{(up)}$ were computed with the STEP of Section 3.1 whereas $\gamma_{k,eff}^{(up)}$ were computed with the EEMCC (Eqs. (28), (29)). On the lower piezoelectric patch, the coefficients verify $\gamma_k^{(down)} = -\gamma_k^{(up)}$.

Bending modes	$k = 1$	$k = 2$	$k = 3$	$k = 4$	$k = 5$	$k = 6$
$f_{k,FE}$ [Hz]	330.34	1097.1	2276.1	3671.4	5805.0	7755.4
$\gamma_k^{(up)}$ [$N V^{-1} kg^{-1/2}$]	2.1245×10^{-2}	1.3383×10^{-1}	1.2116×10^{-2}	-3.2657×10^{-2}	2.3043×10^{-1}	-2.1657×10^{-1}
$\gamma_{k,eff}^{(up)}$ [$N V^{-1} kg^{-1/2}$]	2.2350×10^{-2}	1.4297×10^{-1}	1.2975×10^{-2}	3.4771×10^{-2}	2.4587×10^{-1}	2.3144×10^{-1}
Relative error [%]	5.2	6.83	7.09	6.47	6.70	6.87

Table 8

Numerical values of the cubic coefficients Γ_{jkl}^k , in [$N m^{-3} kg^{-2}$], and of the parametric coefficients $\Lambda_{ik}^{(p)}$, in [$N m^{-1} V^{-1} kg^{-1}$], for the realistic bimorph of Fig. 12. The coupling coefficients verify, for the lower piezoelectric patch, $\gamma_k^{(down)} = -\gamma_k^{(up)}$ and $\Lambda_{ik}^{(down)} = \Lambda_{ik}^{(up)}$.

$k = 1$	$k = 2$	$k = 3$
$\Gamma_{111}^1 = 2.0528 \times 10^{15}$	$\Gamma_{111}^2 = -1.4016 \times 10^{15}$	$\Gamma_{111}^3 = -6.6450 \times 10^{14}$
$\Gamma_{112}^1 = -4.2218 \times 10^{15}$	$\Gamma_{112}^2 = 1.1431 \times 10^{16}$	$\Gamma_{112}^3 = -2.5145 \times 10^{15}$
$\Gamma_{122}^1 = 1.1457 \times 10^{16}$	$\Gamma_{122}^2 = -1.9462 \times 10^{16}$	$\Gamma_{122}^3 = 1.9559 \times 10^{15}$
$\Gamma_{222}^1 = -6.4919 \times 10^{15}$	$\Gamma_{222}^2 = 4.2792 \times 10^{16}$	$\Gamma_{222}^3 = -1.3310 \times 10^{16}$
$\Gamma_{113}^1 = -1.8246 \times 10^{15}$	$\Gamma_{113}^2 = -2.5080 \times 10^{15}$	$\Gamma_{113}^3 = 2.3388 \times 10^{16}$
$\Gamma_{133}^1 = 2.3509 \times 10^{16}$	$\Gamma_{133}^2 = -1.3975 \times 10^{16}$	$\Gamma_{133}^3 = -2.0913 \times 10^{16}$
$\Gamma_{223}^1 = 1.9131 \times 10^{15}$	$\Gamma_{223}^2 = -4.4991 \times 10^{16}$	$\Gamma_{223}^3 = 1.1502 \times 10^{17}$
$\Gamma_{233}^1 = -1.3883 \times 10^{16}$	$\Gamma_{233}^2 = 1.1539 \times 10^{17}$	$\Gamma_{233}^3 = -1.0996 \times 10^{17}$
$\Gamma_{333}^1 = -7.1889 \times 10^{15}$	$\Gamma_{333}^2 = -3.3745 \times 10^{16}$	$\Gamma_{333}^3 = 2.1776 \times 10^{17}$
$\Gamma_{123}^1 = 2.0677 \times 10^{16}$	$\Gamma_{123}^2 = -4.5079 \times 10^{16}$	$\Gamma_{123}^3 = 2.9452 \times 10^{16}$
$\Lambda_{11}^{(up)} = -7.1442 \times 10^2$	$\Lambda_{22}^{(up)} = -3.0695 \times 10^3$	$\Lambda_{33}^{(up)} = -8.5361 \times 10^3$
$\Lambda_{12}^{(up)} = 5.7086 \times 10^2$	$\Lambda_{23}^{(up)} = 1.3541 \times 10^3$	$\Lambda_{13}^{(up)} = 2.5505 \times 10^2$

the hardening behaviour without modal interaction on a reasonable range of amplitude, with an upper bound which corresponds approximately to the thickness of the elastic part (0.5 mm). However, a computation with one mode does not allow for predicting the modal interactions, whose occurrences increase significantly with the number of modes in the basis. Moreover, a convergence effect is also observed with the internal resonances, which are noticeable by the presence of tongues in the free responses. Indeed, a drastic change of curvature of the tongues is observed when the number of modes increases.

The dynamic responses with a parametric excitation are computed by applying a sine voltage of amplitude $V_0 = 800$ V at the upper piezoelectric patch and with short-circuited electrodes at the lower patch. Similarly to the ideal straight beams of Section 5.2, the viscous damping matrix was chosen as $\mathbf{D} = \alpha \mathbf{M}$ with $\alpha = 2\xi\omega_1$ and $\xi = 2\%$. The obtained responses show, without ambiguity, that at least two bending modes must be retained in the basis to predict accurately the maximum amplitude of the response. Indeed, the computation with one mode overestimates more than twice the displacements obtained when at least the second bending mode is added in the basis. This result is in line with the results on the previous test cases (cf. Fig. 10), but with a stronger decrease in the present results. Finally, the curvature does not change significantly with the number of modes in the basis: it is consistent with the results obtained with the free responses, since the maximal amplitude computed with at least two modes does not exceed the thickness of the elastic part.

Finally, both direct and parametric responses are computed with 5 bending modes in the basis with the same voltage signals ($V^{(up)}(t) = V_0 \sin(\Omega t)$ with $V_0 = 800$ V, and $V^{(down)} = 0$), by using both the continuation procedure implemented in Manlab and time integration computed from the full model with Abaqus. The time signals were computed thanks to a Newmark scheme (as in Section 5.2) with time increment $\Delta t = 25 \mu s$, except for the higher

amplitudes ($\max(\mathbf{U}) > 0.6$ mm) for which convergence issues were encountered and for which the time increment was reduced to $\Delta t = 6.25 \mu s$. The responses are depicted in Fig. 14. One can first observe the excellent agreement of our ROM computation with respect to the reference solution obtained by time integrations in Abaqus, for both direct and parametric resonant excitations. Moreover, since the stability of the periodic solutions of the solution branches can be estimated with the Manlab code [76,75], some particular nonlinear dynamics can be easily identified. In particular, the direct response show two main incursions on the stable upper branch, which are due to the effect of two distinct internal resonances, since they follow the tongues of the free responses. By looking at the harmonic content of each modal coordinate of the ROM, one can show that a 1:3 internal resonance with mode 2, that means an exchange of energy between the first harmonic of mode 1 and the third harmonic of mode 2, is observed around $\Omega \simeq 1.22\omega_1$. Other internal resonances, a 1:9 with mode 4 and a 1:5 with mode 3, are also observed respectively around $\Omega \simeq 1.28\omega_1$ and $\Omega \simeq 1.57\omega_1$. These modal interactions leads to quasi-periodic oscillations, that are theoretically predicted since the periodic solution loses its stability through Neimark-Sacker bifurcations. The time integration with Abaqus predicts those quasiperiodic responses with beatings in the displacement signals, clearly visible in Fig. 14(c), at frequencies $\Omega = 1.24\omega_1$ and $\Omega = 1.26\omega_1$.

It must be noted that the voltage $V_0 = 800$ V used in the simulations is large (it corresponds to an electric field of 1.6 kV/mm in the piezoelectric layer, not far from the coercive field of classical macro PZT ceramics, of the order of 2 kV/mm [80]). In a real application, material piezoelectric nonlinearities would be observed. In our test case, this voltage was chosen in order to observe significant geometrically nonlinear behaviour. Since those nonlinearities are related to the amplitude of the motion, they would be equally observed with lower voltage by reducing the damping ratio.

7. Conclusion

In this work, we presented a complete and efficient strategy to compute the nonlinear free and forced frequency responses of thin structures with piezoelectric patches, subjected to geometrical nonlinearities, using a reduced order model (ROM) and a continuation method to obtain the periodic responses and their stability. The ROM includes an efficient coupling to any electrical circuit, since the electrical degrees of freedom are global (the voltages between the electrodes of the piezoelectric patches and the associated electric charges) and because both converse and direct piezoelectric effects are considered. The main originality of our approach is that our ROM naturally includes the terms that are related to parametric excitations of the structure. Those so-called parametric terms are second order nonlinear terms that couple the displacements and the piezoelectric voltages.

The proposed numerical strategy is composed of two steps. The first one is the preliminary computation of the coefficients of the reduced order model using a finite element (FE) code in a non-

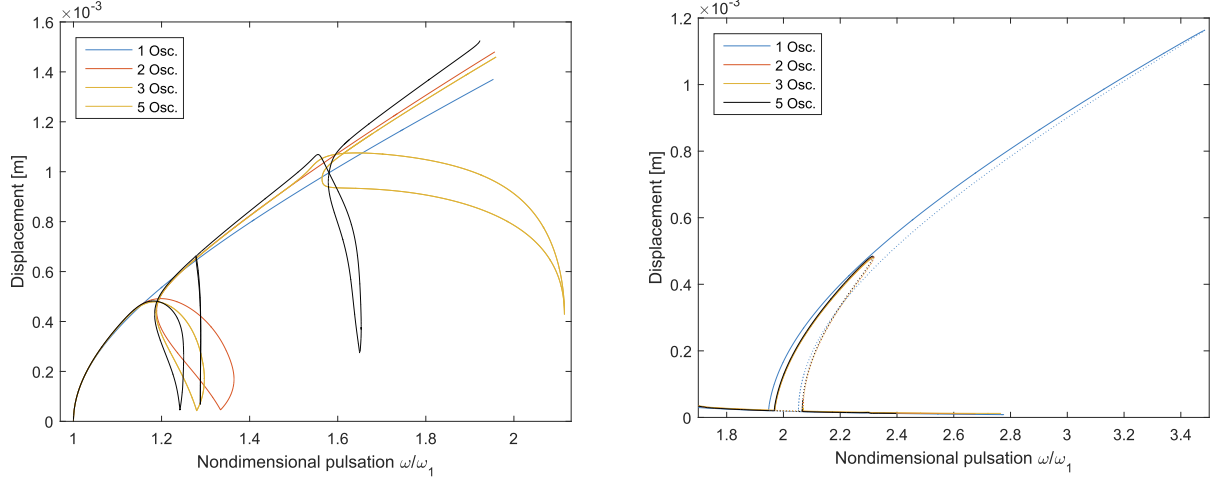


Fig. 13. Nonlinear free (left) and parametric (right) responses of the realistic bimorph of Fig. 12, computed with Manlab, with increasing number of bending modes in the ROM. All computations are performed with 10 harmonics in the HBM and the maximum transverse displacement over one period, at the center of the beam, is shown.

intrusive manner. Only standard modal analyses and nonlinear static computations with prescribed displacements are used. Any FE code can be used as long as it includes piezoelectric and geometrical nonlinearities capabilities. In a second step, the ROM can be used either with a standard time integration scheme or with a continuation method to obtain the dynamics of the system.

Because we used a FE discretization with 3D degrees of freedom, instead of laminated beam or plate models, a particularly slow modal convergence was observed because of couplings between bending modes and high order membrane and thickness modes. We proposed a special strategy, called the M-STEP, to overcome this difficulty and to automatically condense all those slave modes into the bending motion. At the moment, it is restricted to structures with a transverse symmetry, to avoid linear membrane/ bending coupling. The M-STEP can also be applied to symmetric laminated beam/plate FE (such as in [48]). In this case, since no thickness modes are present, the M-STEP would naturally embed the coupling of the bending with the membrane modes. For non-symmetric structures, equivalent results are not available at the moment. Among others, that includes modal derivatives [51] or stress manifolds [16], recent developments using direct normal form computations seems promising [56,57]. It however remains to adapt them to the present electromechanical structure.

The procedure was validated on three test cases of increasing geometrical complexity, with comparisons to analytical solutions as well as to reference results obtained with time integrations in the FE code. A perfect agreement was obtained, fully validating our strategy.

This paper was also a mean of investigating the nonlinear response of piezoelectric structures, that can be complex because of modal interactions, that leads to instabilities of the periodic solution and exchanges of energy between modes. Moreover, the parametric response of the structures was also particularly addressed. An unexpected result was the huge dependence of the parametric resonance on the number of bending modes retained in the ROM. For our realistic third test case, it was shown that considering a ROM truncated to only one bending mode (as it is usually done) leads to a large error (of about 100%) in the amplitude of the parametric resonance. This error was corrected by adding a second mode in the expansion basis.

As compared to the time integration of the full FE model, the only procedure available currently in standard FE codes, our strategy has two advantages. The first one is the computation time. Computing the full frequency response curve with Manlab takes a few minutes on a standard personal computer whereas it costed

us several days on for the time integrations of the full FE model. The latter are also not straightforward since the time integrator can become unstable, because of the stiff nature of the system. Secondly, using continuation methods, such as the one implemented in Manlab, offers all the refinement of modern nonlinear dynamics tools. It enables to identify the instabilities, to compute the unstable parts, to naturally understand the modal energy exchanges and also to compute the free responses (the backbone curves, equivalent to the nonlinear modes of the system) that most of the time give the skeleton of the dynamics.

Declaration of Competing Interest

The authors declare that they have no known competing financial interests or personal relationships that could have appeared to influence the work reported in this paper.

Acknowledgements

The authors acknowledge the Arts et Métiers High Performance Computing Center Cassiopee with which the Abaqus time integrations were performed. The French Ministry of Research is thanked for the financial support of this study, through the Ph.D. Grant of the first author.

Appendix A. Variational formulation and finite element discretization

This appendix is devoted to the justification of Eqs. (7) from Eqs. (6b). For this, we first write the variation of the strain as:

$$\delta\varepsilon_{ij} = \frac{1}{2} (\delta u_{ij} + \delta u_{ji} + u_{k,i} \delta u_{kj} + \delta u_{k,i} u_{kj}). \quad (\text{A.1})$$

Eqs. (6a) and (6b) are rewritten in Voigt notation, *i.e.* by considering the symmetry properties of the tensors $\varepsilon_{ij}, \pi_{ij}, c_{ijkl}^E, e_{kij}$ with $i, j, k \in [1, 3]$, respectively replaced by the vectors $\varepsilon_i, \pi_i, i \in [1, 6]$ and matrices c_{ij}^E, e_{ki} with $i, j \in [1, 6]$ and $k \in [1, 3]$. The strain tensor and its variation defined in Eq. (A.1) can be split in linear and non-linear terms:

$$\varepsilon_i(u) = \varepsilon_i^{(1)}(u) + \varepsilon_i^{(2)}(u, u) \quad (\text{A.2a})$$

$$\delta\varepsilon_i(u, \delta u) = \varepsilon_i^{(1)}(\delta u) + \varepsilon_i^{(3)}(u, \delta u). \quad (\text{A.2b})$$

with the following explicit forms of $\varepsilon_i^{(1)}, \varepsilon_i^{(2)}$ and $\varepsilon_i^{(3)}$:

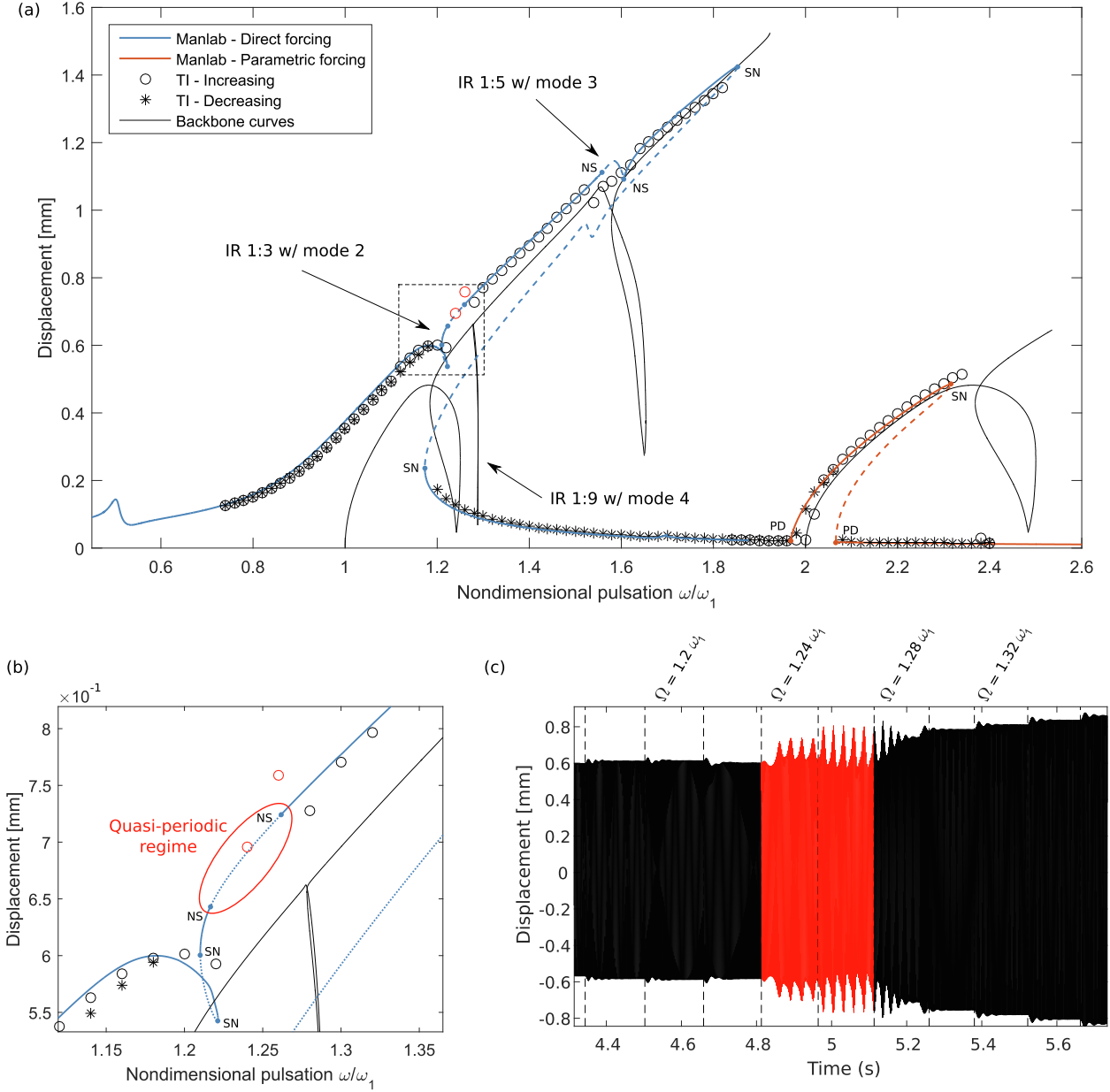


Fig. 14. (a) Frequency response of the first resonance of the realistic bimorph of Fig. 12, obtained with direct and parametric excitation, computed with Manlab with 18 harmonics in the HBM, and time integrations from the full finite element model in Abaqus. IR: internal resonance; NS: Neimark-Sacker bifurcation; PD: Period doubling bifurcation (b) Zoom on the first incursion in the directly excited response around the 1:3 internal resonance with mode 2, and (c) corresponding displacement signal computed by time integration. The maximum transverse displacement over one period, at the center of the beam, is shown.

$$\varepsilon_i^{(1)}(u) = \begin{bmatrix} u_{1,1} \\ u_{2,2} \\ u_{3,3} \\ u_{2,3} + u_{3,2} \\ u_{1,3} + u_{3,1} \\ u_{1,2} + u_{2,1} \end{bmatrix} \quad \varepsilon_i^{(2)}(u) = \begin{bmatrix} \frac{1}{2}(u_{1,1}^2 + u_{2,1}^2 + u_{3,1}^2) \\ \frac{1}{2}(u_{1,2}^2 + u_{2,2}^2 + u_{3,2}^2) \\ \frac{1}{2}(u_{1,3}^2 + u_{2,3}^2 + u_{3,3}^2) \\ u_{1,2}u_{1,3} + u_{2,2}u_{2,3} + u_{3,2}u_{3,3} \\ u_{1,1}u_{1,3} + u_{2,1}u_{2,3} + u_{3,1}u_{3,3} \\ u_{1,1}u_{1,2} + u_{2,1}u_{2,2} + u_{3,1}u_{3,2} \end{bmatrix}$$

$$\varepsilon_i^{(3)}(u, \delta u) = \begin{bmatrix} u_{1,1}\delta u_{1,1} + u_{2,1}\delta u_{2,1} + u_{3,1}\delta u_{3,1} \\ u_{1,2}\delta u_{1,2} + u_{2,2}\delta u_{2,2} + u_{3,2}\delta u_{3,2} \\ u_{1,3}\delta u_{1,3} + u_{2,3}\delta u_{2,3} + u_{3,3}\delta u_{3,3} \\ u_{1,2}\delta u_{1,3} + u_{2,2}\delta u_{2,3} + u_{3,2}\delta u_{3,3} + \delta u_{1,2}u_{1,3} + u_{2,2}u_{2,3} + \delta u_{3,2}u_{3,3} \\ u_{1,1}\delta u_{1,3} + u_{2,1}\delta u_{2,3} + u_{3,1}\delta u_{3,3} + \delta u_{1,1}u_{1,3} + \delta u_{2,1}u_{2,3} + \delta u_{3,1}u_{3,3} \\ u_{1,1}\delta u_{1,2} + u_{2,1}\delta u_{2,2} + u_{3,1}\delta u_{3,2} + \delta u_{1,1}u_{1,2} + \delta u_{2,1}u_{2,2} + \delta u_{3,1}u_{3,2} \end{bmatrix}$$

which thus allows for writing $\varepsilon_i^{(1)} = D_{ij}^{(1)}u_j$, $\varepsilon_i^{(2)} = D_{ij}^{(2)}(u)u_j$ and $\varepsilon_i^{(3)} = D_{ij}^{(3)}(u)\delta u_j$ with the operators defined by:

$$D_{ij}^{(1)} = \begin{bmatrix} \frac{\partial}{\partial x_1} & 0 & 0 \\ 0 & \frac{\partial}{\partial x_2} & 0 \\ 0 & 0 & \frac{\partial}{\partial x_3} \\ 0 & \frac{\partial}{\partial x_3} & \frac{\partial}{\partial x_2} \\ \frac{\partial}{\partial x_3} & 0 & \frac{\partial}{\partial x_1} \\ \frac{\partial}{\partial x_2} & \frac{\partial}{\partial x_1} & 0 \end{bmatrix}$$

$$D_{ij}^{(3)}(u) = 2D_{ij}^{(2)}(u) = \begin{bmatrix} u_{1,1}\frac{\partial}{\partial x_1} & u_{2,1}\frac{\partial}{\partial x_1} & u_{3,1}\frac{\partial}{\partial x_1} \\ u_{1,2}\frac{\partial}{\partial x_2} & u_{2,2}\frac{\partial}{\partial x_2} & u_{3,2}\frac{\partial}{\partial x_2} \\ u_{1,3}\frac{\partial}{\partial x_3} & u_{2,3}\frac{\partial}{\partial x_3} & u_{3,3}\frac{\partial}{\partial x_3} \\ u_{1,2}\frac{\partial}{\partial x_3} + u_{1,3}\frac{\partial}{\partial x_2} & u_{2,2}\frac{\partial}{\partial x_3} + u_{2,3}\frac{\partial}{\partial x_2} & u_{3,2}\frac{\partial}{\partial x_3} + u_{3,3}\frac{\partial}{\partial x_2} \\ u_{1,1}\frac{\partial}{\partial x_3} + u_{1,3}\frac{\partial}{\partial x_1} & u_{2,1}\frac{\partial}{\partial x_3} + u_{2,3}\frac{\partial}{\partial x_1} & u_{3,1}\frac{\partial}{\partial x_3} + u_{3,3}\frac{\partial}{\partial x_1} \\ u_{1,1}\frac{\partial}{\partial x_2} + u_{1,2}\frac{\partial}{\partial x_1} & u_{2,1}\frac{\partial}{\partial x_2} + u_{2,2}\frac{\partial}{\partial x_1} & u_{3,1}\frac{\partial}{\partial x_2} + u_{3,2}\frac{\partial}{\partial x_1} \end{bmatrix}$$

which makes appear that $D_{ij}^{(2)}(u) = \frac{1}{2}D_{ij}^{(3)}(u)$. In the finite element context, let U_k, Ψ_k be the nodal displacements and electric potentials and $N_{ij}(Y), H_k(Y)$ the corresponding interpolation functions, such that $u_i(Y) = N_{ik}(Y)U_k$ and $\psi(Y) = H_k(Y)\Psi_k$. We now rewrite the variational formulation with the introduction of the operators $B_{ik}^{(0)} = H_{k,i}, B_{ij}^{(1)} = D_{ik}^{(1)}N_{kj}$ and

$$B_{ijk}^{(2)} = \begin{bmatrix} \frac{\partial N_{ij}}{\partial Y_1} \frac{\partial N_{ik}}{\partial Y_1} \\ \frac{\partial N_{ij}}{\partial Y_2} \frac{\partial N_{ik}}{\partial Y_2} \\ \frac{\partial N_{ij}}{\partial Y_3} \frac{\partial N_{ik}}{\partial Y_3} \\ \frac{\partial N_{ij}}{\partial Y_2} \frac{\partial N_{ik}}{\partial Y_3} + \frac{\partial N_{ij}}{\partial Y_3} \frac{\partial N_{ik}}{\partial Y_2} \\ \frac{\partial N_{ij}}{\partial Y_3} \frac{\partial N_{ik}}{\partial Y_1} + \frac{\partial N_{ij}}{\partial Y_1} \frac{\partial N_{ik}}{\partial Y_3} \\ \frac{\partial N_{ij}}{\partial Y_2} \frac{\partial N_{ik}}{\partial Y_1} + \frac{\partial N_{ij}}{\partial Y_1} \frac{\partial N_{ik}}{\partial Y_2} \end{bmatrix} \quad (\text{A.3})$$

such that $E_i = -\psi_{,i} = -B_{ik}^{(0)}\Psi_k, \delta E_i = -B_{ik}^{(0)}\delta\Psi_k, \varepsilon_i(U) = B_{ij}^{(1)}U_j + \frac{1}{2}B_{ijk}^{(2)}U_jU_k$ and $\delta\varepsilon_i(U) = B_{ij}^{(1)}\delta U_j + B_{ijk}^{(2)}U_k\delta U_j$. In the above equation, each row of the matrix correspond to a value of index $i=1, \dots, 6$. Introducing these variables in the internal work of Eqs. (6a) and (6b) leads to the matricial formulation of Eq. (7), in which the following matrices and tensors have been defined:

- $K_{klm}^{(2)} = \int_{\Omega} c_{ij} \left[\frac{1}{2}B_{ijk}^{(2)}B_{il}^{(1)} + B_{jk}^{(1)}B_{ilm}^{(2)} \right] d\Omega$ and $K_{klmn}^{(3)} = \int_{\Omega} c_{ij} \left[\frac{1}{2}B_{ijkl}^{(2)}B_{ilmn}^{(2)} \right] d\Omega$ are the quadratic and cubic components of the tangent stiffness matrix
- $K_{ij}^c = \int_{\Omega_p} e_{kl}B_{ki}^{(0)}B_{lj}^{(1)} d\Omega \forall p \in [1, P]$ denotes the electromechanical coupling matrix
- $L_{klm}^c = \int_{\Omega_p} e_{ij}B_{ik}^{(0)}B_{jlm}^{(2)} d\Omega \forall p \in [1, P]$ is the third-order tensor taking into account both piezoelectric coupling and geometric nonlinearities, also called the parametric tensor.
- $K_{ij}^e = \int_{\Omega} \epsilon_{kl}B_{ki}^{(0)}B_{lj}^{(0)} d\Omega$ is the dielectric matrix.

The tensor L_{klm}^c is symmetric ($L_{klm}^c = L_{kml}^c$), because of the similar symmetry property of the operator $B_{ijk}^{(2)}$, highlighted in Eq. (A.3).

Appendix B. Condensation of the electric dofs and equipotentiality properties

To simplify the writing, we only detail the derivations in the case of a structure equipped with only one piezoelectric patch, bearing in mind that all derivations can be generalized to the case of an arbitrary number of patches.

As explained in the main text, the piezoelectric patches are covered with conducting electrodes. Two main and well-known consequences of the Gauss's law are used: first, the charges at the internal nodes are zero, since the free charges are only concentrated on the common boundaries of the piezoelectric patch and its electrodes, in the form of surface densities. These charges are free to move on those surfaces because of the conducting electrode [81]. Secondly, the global charge in the electrodes are opposite on the two electrodes. It is now convenient to rewrite Eqs. (7) by separating the electric degrees of freedom of the piezoelectric patches, considering first the nodes placed on the upper/lower electrodes and secondly the nodes inside the patches. We refer to the upper, lower and internal nodes with superscript indices $+, -, 0$. The matrices $K_{ik}^c, L_{ikl}^c U_l$ and K_{ik}^e are then separated following this partition: let $K_{ik}^{c+}, K_{ik}^{c-}, K_{ik}^{c0}$ be the submatrices of

$K_{ik}^{c+}, L_{ikl}^{m+} U_l^+, L_{ikl}^{m-} U_l^-, L_{ikl}^{m0} U_l^0$ the submatrices of $L_{ikl}^c U_l$, and $K_{ik}^{e+}, K_{ik}^{e-}, K_{ik}^{e0}, K_{ik}^{e+}, K_{ik}^{e-}, K_{ik}^{e0}$ the submatrices of K_{ik}^e , such that Eq. (7) becomes:

$$M_{ij}\ddot{U}_j + K_{ij}^m U_j + f_i^f(U) + (K_{ik}^{m+} + L_{ikl}^{m+} U_l^+) \Psi_k^+ + (K_{ik}^{m-} + L_{ikl}^{m-} U_l^-) \Psi_k^- + (K_{ik}^{m0} + L_{ikl}^{m0} U_l^0) \Psi_k^0 = f_i^{\text{ext}} \quad (\text{B.1a})$$

$$- \left(K_{jk}^{m+} + \frac{1}{2} L_{jkl}^{m+} U_l^+ \right) U_j^+ + K_{kr}^{m+} \Psi_r^+ + K_{kr}^{m-} \Psi_r^- + K_{kr}^{m0} \Psi_r^0 = q_k^+ \quad (\text{B.1b})$$

$$- \left(K_{jk}^{m-} + \frac{1}{2} L_{jkm}^{m-} U_m^- \right) U_j^- + K_{rk}^{m-} \Psi_r^+ + K_{rk}^{m-} \Psi_r^- + K_{rk}^{m0} \Psi_r^0 = q_k^- \quad (\text{B.1c})$$

$$- \left(K_{jk}^{m0} + \frac{1}{2} L_{jkm}^{m0} U_m^0 \right) U_j^0 + K_{rk}^{m0} \Psi_r^+ + K_{rk}^{m0} \Psi_r^- + K_{rk}^{m0} \Psi_r^0 = 0 \quad (\text{B.1d})$$

with q_k^+ and q_k^- the nodal surface charge densities on S^+ and S^- .

Since no external charge can be applied inside the piezoelectric patches, Eq. (B.1d) has a zero second member and the potential internal to the piezoelectric patch, sometimes called the induced potential [82], can be written

$\Psi_k^0 = (K^{00})_{kr}^{-1} \left((K_{jr}^{m0} + L_{jrs}^{m0} U_s^0) U_j^0 - K_{nr}^{m0} \Psi_n^+ - K_{nr}^{m0} \Psi_n^- \right)$, with $(\bullet)_{ij}^{-1}$ the inverse matrix verifying $(\bullet)_{ij}^{-1} (\bullet)_{jk} = \delta_{ik}$. It can then be eliminated (condensed) into the other Eqs. (B.1a), (B.1b) and (B.1c), thus leading to:

$$M_{ij}\ddot{U}_j + K_{ij} U_j + f_i(U) + \left(\widehat{K}_{ik}^{m+} + \widehat{L}_{ikl}^{m+} U_l^+ \right) \Psi_k^+ + \left(\widehat{K}_{ik}^{m-} + \widehat{L}_{ikl}^{m-} U_l^- \right) \Psi_k^- = f_i^{\text{ext}} \quad (\text{B.2a})$$

$$- \left(\widehat{K}_{jk}^{m+} + \frac{1}{2} \widehat{L}_{jkl}^{m+} U_l^+ \right) U_j^+ + \widehat{K}_{kr}^{m+} \Psi_r^+ + \widehat{K}_{kr}^{m-} \Psi_r^- = q_k^+ \quad (\text{B.2b})$$

$$- \left(\widehat{K}_{jk}^{m-} + \frac{1}{2} \widehat{L}_{jkl}^{m-} U_l^- \right) U_j^- + \widehat{K}_{rk}^{m-} \Psi_r^+ + \widehat{K}_{rk}^{m-} \Psi_r^- = q_k^-, \quad (\text{B.2c})$$

where the corrected matrices write:

$$\begin{aligned} f_i(U) &= f_i^f(U) + \widehat{K}_{ijs}^{(2)} U_s^0 U_j^0 + \widehat{K}_{ijs}^{(3)} U_s^0 U_l^0 U_j^0 \\ \widehat{K}_{ijs}^{(2)} &= K_{ik}^{m0} (K^{00})_{kr}^{-1} L_{jrs}^{m0} + L_{iks}^{m0} (K^{00})_{kr}^{-1} K_{jr}^{m0}, \quad \widehat{K}_{ijs}^{(3)} = L_{ijs}^{m0} (K^{00})_{kr}^{-1} L_{jrs}^{m0} \\ K_{ij} &= K_{ij}^m + K_{ik}^{m0} (K^{00})_{kr}^{-1} K_{jr}^{m0} \\ \widehat{K}_{ik}^{m+} &= -K_{il}^{m0} (K^{00})_{rs}^{-1} K_{rs}^{m0}, \quad \widehat{K}_{ik}^{m-} = -K_{il}^{m0} (K^{00})_{rs}^{-1} K_{rs}^{m0} \\ \widehat{L}_{ikl}^{m+} &= L_{ikl}^{m+} - L_{itl}^{m0} (K^{00})_{rs}^{-1} K_{rs}^{m0}, \quad \widehat{L}_{ikl}^{m-} = L_{ikl}^{m-} - L_{itl}^{m0} (K^{00})_{rs}^{-1} K_{rs}^{m0} \\ \widehat{K}_{kl}^{m+} &= K_{kl}^{m+} - K_{kr}^{m0} (K^{00})_{rs}^{-1} K_{ls}^{m0}, \quad \widehat{K}_{kl}^{m-} = K_{kl}^{m-} - K_{kr}^{m0} (K^{00})_{rs}^{-1} K_{ls}^{m0} \\ \widehat{K}_{kl}^{m0} &= K_{kl}^{m0} - K_{kr}^{m0} (K^{00})_{rs}^{-1} K_{ls}^{m0}. \end{aligned} \quad (\text{B.3})$$

On each electrode, since the potential is uniform, this equipotentiality property can be written:

$$\Psi_k^+ = \begin{bmatrix} 1 \\ \vdots \\ 1 \end{bmatrix} \Psi^+, \quad \Psi_k^- = \begin{bmatrix} 1 \\ \vdots \\ 1 \end{bmatrix} \Psi^-.$$

Consequently, Eq. (B.2a) is simplified as:

$$M_{ij}\ddot{U}_j + K_{ij} U_j + f_i(U) + (f_i^{m+} + P_{il}^{m+} U_l^+) \Psi^+ + (f_i^{m-} + P_{il}^{m-} U_l^-) \Psi^- = f_i^{\text{ext}} \quad (\text{B.4})$$

$$f_i^{m+} = \sum_{k=1}^{N^+} \widehat{K}_{ik}^{m+}, \quad f_i^{m-} = \sum_{k=1}^{N^-} \widehat{K}_{ik}^{m-}, \quad P_{il}^{m+} = \sum_{k=1}^{N^+} \widehat{L}_{ikl}^{m+},$$

$$P_{il}^{m-} = \sum_{k=1}^{N^-} \widehat{L}_{ikl}^{m-}.$$

These terms also appear by summing the terms of Eqs. (B.2b) and (B.2c), thus leading to:

$$-\left(f_j^{m+} + \frac{1}{2}P_{jl}^{m+}U_l^+\right)U_j^+ + C^{++}\Psi^+ + C^{+-}\Psi^- = Q^+ \quad (\text{B.6a})$$

$$-\left(f_j^{m-} + \frac{1}{2}P_{jl}^{m-}U_l^-\right)U_j^- + C^{+-}\Psi^+ + C^{--}\Psi^- = Q^-, \quad (\text{B.6b})$$

with

$$C^{++} = \sum_{k=1}^{N^+} \sum_{l=1}^{N^+} K_{kl}^{++}, \quad C^{+-} = \sum_{k=1}^{N^+} \sum_{l=1}^{N^-} K_{kl}^{+-}, \quad C^{--} = \sum_{k=1}^{N^-} \sum_{l=1}^{N^-} K_{kl}^{--},$$

and in which the global electric charge in each electrode is expressed with the following formulae:

$$Q^+ = \sum_{k=1}^{N^+} q_k^+, \quad Q^- = \sum_{k=1}^{N^-} q_k^-. \quad (\text{B.7})$$

Finally, Eqs. (B.4), (B.6b) and (B.6b) can further be simplified as follows:

- a consequence of the Gauss's law is $Q^+ = -Q^- = Q$
- it can be shown that $C^{--} = C^{++} = -C^{+-} = C$ by introducing the voltage $V = \Psi^+ - \Psi^-$ and denoting it with different references (for instance $\Psi^- = 0, \Psi^+ = V$ and $\Psi^- = -V, \Psi^+ = 0$). This term denote the capacity, defined for rectangular patches as $C = \epsilon_{33}L_p b_p / h_p$ [41] with L_p, b_p, h_p the length, width and thickness of the patch.
- the relationship $f_j^{m+} + \frac{1}{2}P_{jl}^{m+}U_l^+ = -\left(f_j^{m-} + \frac{1}{2}P_{jl}^{m-}U_l^-\right)$ is then straightforward.

Eqs. (B.6a) and (B.6b) are thus equivalent. Finally, Eq. (B.1) is written as:

$$M_{ij}\ddot{U}_j + K_{ij}U_j + f_i(U) + (f_i^c + P_{ij}U_j)V = f_i^{\text{ext}} \quad (\text{B.8a})$$

$$-\left(f_i^c + \frac{1}{2}P_{ij}U_j\right)U_i + CV = Q \quad (\text{B.8b})$$

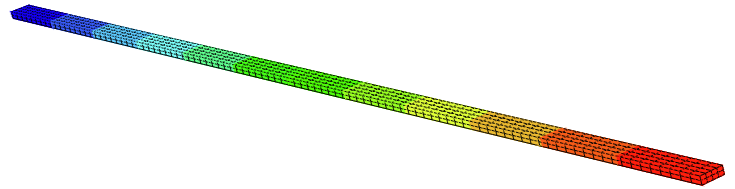
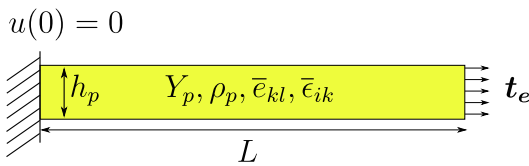


Fig. C.15. (a) Homogeneous, piezoelectric beam with load (traction applied on the second end) and boundary condition (clamped at the first end). (b) Result of the traction test on Abaqus with short-circuited electric BCs. The colors correspond to the displacements in the axial direction. (For interpretation of the references to colour in this figure legend, the reader is referred to the web version of this article.)

Table C.9

Parameters of the numerical model for the material NCE51. In order of appearance: dimensions, density, piezoelectric and dielectric coefficients, elastic constants at zero electric field.

L (m)	b (m)	h_p (m)	ρ_p (kg.m ⁻³)	$e_{311} = e_{322}$ (C.m ⁻²)	e_{333}	$e_{123} = e_{113}$	
1	0.02	0.007	7850	-6.06	17.2	13.7	
$\epsilon_{11}^e = \epsilon_{22}^e$ (nF/m)	ϵ_{33}^e	$c_{1111}^E = c_{2222}^E$ (GPa)	c_{3333}^E	c_{1122}^E	$c_{1133}^E = c_{2233}^E$	$c_{2323}^E = c_{1313}^E$	c_{1212}^E
8.02	7.29	134	121	88.9	90.9	20.5	22.4

with the electrical Eq. (B.8b) written on the upper electrode only, and where the linear and nonlinear coupling vector and matrix are denoted by $f_j^c = f_j^{m+}$ and $P_{ij}^c = P_{ij}^{m+}$. The procedure can be generalized for an arbitrary number of P piezoelectric patches, it only needs to consider supplementary and equation lines in Eqs. (B.1d). With bold notation, f_j^c and P_{ij}^c on the p^{th} patch are respectively denoted with $\mathbf{f}_j^{c(p)}$ and $\mathbf{P}_c^{(p)}$. It thus leads to the general system of Eqs. (8).

Appendix C. Validation test case for the computation of the electric charge

We aim to provide a reference result for computation of the electric charge, as proposed by Eq. (B.7). At this end, this section presents an analytical and a numerical computation of the charge in a traction test of a homogeneous piezoelectric beam, as shown in Fig. C.15. An external normal force is applied at the free end of a cantilever, homogeneous beam ($u(0) = 0, w(0) = 0$). Since no bending is applied, there is no induced potential with a quadratic form [82], the solutions in charge and displacement are exact. Moreover, with short-circuited electrodes, only the first term of Eq. (E.4) is involved and the electric charge which appear in the electrodes writes:

$$Q = -\Xi u(L). \quad (\text{C.1})$$

The equilibrium equation reduces to $N_x = 0$: it leads to a constant internal axial force, which equals the external force $N_e = bh_p t_e$ applied at the free end, with t_e a surface traction, b the width of the beam and h_p its thickness. According to Eq. (E.3a), it leads to:

$$\int_0^L N dx = LN_e = Lbh_p t_e = Y_p bh_p u(L). \quad (\text{C.2})$$

By combining Eqs. (C.1) and (C.2) and using $\Xi = b\bar{e}_{31}$, the resulting charge writes:

$$Q = \frac{bL\bar{e}_{31}}{Y_p} t_e \quad (\text{C.3})$$

For our numerical test, the piezoelectric material is NCE51 [83]: the constants of the full piezoelectric law given in Table C.9 are assigned to the beam in the numerical model. The corresponding modified constants used in Eq. (E.2) are presented in Table C.10. We apply a uniform surface traction of $t_e = 10 \times 10^3$ Pa at the free

Table C.10

Parameters of the modified constants of Eq. (E.2) corresponding to the properties of Table C.9.

Y_p (GPa)	$\bar{\epsilon}_{31}$ (C.m ⁻²)	$\bar{\epsilon}_{33}^e$ (nF.m ⁻¹)
59.25	-13.03	15.95

Table C.11

Electric charges computed with numerical and analytical methods.

	Analytical (Eq. (C.3))	Numeric (Eq. (B.7))	Error (%)
El. charge Q [C]	4.398e ⁻⁸	4.396e ⁻⁸	0.045

end of the beam, which leads to the results of Table C.11, which shows a negligible error.

Appendix D. Static condensation of the cubic and parametric coefficients

In the section, we detail the static condensation that leads to replace Eqs. (19a-c) by (21a-b). First, the partial correction factor \mathcal{G}_{ijl}^{ks} for the cubic coefficients is written [15,49]:

$$\mathcal{G}_{ijk}^{rs} = \begin{cases} \frac{a_{is}^k a_{jl}^s}{\omega_s^2} + \frac{a_{js}^k a_{il}^s}{\omega_s^2} + \frac{a_{ls}^k a_{ij}^s}{\omega_s^2} & i < j < l \\ \frac{a_{is}^k a_{jl}^s}{\omega_s^2} + \frac{a_{ls}^k a_{ij}^s}{\omega_s^2} & i = j < l \\ \frac{a_{is}^k a_{jl}^s}{\omega_s^2} + \frac{a_{ls}^k a_{ij}^s}{\omega_s^2} & i < j = l \\ \frac{a_{is}^k a_{il}^s}{\omega_s^2} & i = j = l. \end{cases}$$

We now compute the condensed parametric coefficients, which can be obtained by introducing Eq. (20) either in Eq. (19a) or in Eq. (19c). We denote by $(\bar{\Lambda}_{ik}^{(p)}, \hat{\Lambda}_{ik}^{(p)})$ the corresponding condensed coefficients and $(\bar{\mathcal{F}}_{ik}^{s(p)}, \hat{\mathcal{F}}_{ik}^{s(p)})$ their respective correction factor. They are written such that:

$$\bar{\Lambda}_{ik}^{(p)} = \Theta_{ik} - \sum_{s=N_B+1}^N \bar{\mathcal{F}}_{ik}^{s(p)} = \hat{\Lambda}_{ik}^{(p)} = \Theta_{ik} - \sum_{s=N_B+1}^N \hat{\mathcal{F}}_{ik}^{s(p)} \quad (D.1)$$

The first correction factor for the parametric coefficient $\bar{\mathcal{F}}_{ik}^{s(p)}$ has for expression:

$$\bar{\mathcal{F}}_{ik}^{s(p)} = \frac{\chi_s^{(p)} a_{ik}^s}{\omega_s^2} \quad (D.2)$$

To express the second correction factor $\hat{\mathcal{F}}_{ik}^{s(p)}$, we first need to distinguish the upper triangular form quadratic coefficients \bar{a}_{ij}^s from the non-upper ones \bar{a}_{ji}^s , they particularly verify $a_{ii}^s = \bar{a}_{ii}^s$ and $a_{ij}^s = \bar{a}_{ij}^s + \bar{a}_{ji}^s$ if $j > i$. We now rewrite the quadratic terms of Eq. (Appendix D) by considering both the cases of different and identical bending modes i, j in the summation:

$$\eta_s = -\omega_s^{-2} \left(\sum_{i=1}^{N_B} a_{ii}^s x_i^2 + \sum_{i=1}^{N_B} \sum_{j>i}^{N_B} \frac{a_{ij}^s}{2} x_i x_j + \sum_{i=1}^{N_B} \sum_{j=1}^{j<i} \frac{a_{ij}^s}{2} x_i x_j + \sum_{p=1}^P \chi_s^{(p)} V^{(p)} \right).$$

We thus identify the second correction factor for the parametric coefficients as:

$$\hat{\mathcal{F}}_{ik}^{s(p)} = \begin{cases} \frac{a_{ii}^s \chi_s^{(p)}}{\omega_s^2} & i = j \\ \frac{a_{ij}^s \chi_s^{(p)}}{2\omega_s^2} & j \neq i \end{cases} \quad (D.3)$$

At this stage, it is convenient to use the following symmetry property of the non-upper triangular coefficients, fulfilled provided that the nonlinear stiffness derives from a potential [12]:

$$\bar{a}_{is}^k = 2\bar{a}_{ij}^s \quad \forall i, j \in [1, N_B]. \quad (D.4)$$

which is rewritten on the upper triangular form:

$$a_{is}^k = 2a_{ii}^s \quad \forall i \in [1, N_B], \quad a_{is}^k = a_{ij}^s \text{ if } j > i. \quad (D.5)$$

Introducing Eq. (D.5) in Eq. (D.3) verify the relationship $\hat{\mathcal{F}}_{ik}^{s(p)} = \bar{\mathcal{F}}_{ik}^{s(p)}$. It justifies using a single symbol $\bar{\mathcal{F}}_{ik}^{s(p)}$ in the main text (Eq. (22b)).

Appendix E. Analytical beam model

In this section, we present an analytical model of a symmetric piezoelectric beam with rectangular cross-section. This model is based on the assumptions and notations of [84], and we propose here an extension to the geometrically nonlinear case, by considering the following von Kármán displacement strain law:

$$\epsilon_{xx} = u_{,x} - z w_{,xx} + \frac{1}{2} (w_{,x})^2 \quad (E.1)$$

with ϵ_{xx} the uniaxial strain. u, w are the axial and transverse displacement of a point of the middle line of the beam, respectively defined in the x - and z -directions. The voltage writes $V^{(p)}(t) = -h_p E_z^{(p)}(t)$, with $h_p = z_p - z_{p-1}$ the thickness of a piezoelectric patch. Considering a predominant "31" piezoelectric effect, the reduced constitutive law at the r^{th} layer writes:

$$\pi_{xx} = Y^{(r)} \epsilon_{xx} - \bar{\epsilon}_{31} E_z \quad (E.2a)$$

$$D_z = \bar{\epsilon}_{31} \epsilon_{xx} + \bar{\epsilon}_{33} E_z. \quad (E.2b)$$

with $\bar{\epsilon}_{31} = 0$ for an elastic material. The equivalent Young modulus at zero electric field $Y^{(r)}$, modified piezoelectric constant $\bar{\epsilon}_{31}$ and modified electric permittivity $\bar{\epsilon}_{33}$ of a piezoelectric material can be found from the full constitutive law and material constants provided in Table 1 or C.9 using explicit expressions based on plain stress assumptions [41]. The axial force N and the bending moment M are obtained by integrating Eq. (E.2a) across the cross-section. It leads to:

$$N = A \left[u_{,x} + \frac{1}{2} (w_{,x})^2 \right] + \sum_{p \in \mathcal{P}} \Xi^{(p)} V^{(p)} \quad (E.3a)$$

$$M = -D w_{,xx} + \sum_{p \in \mathcal{P}} \Pi^{(p)} V^{(p)} \quad (E.3b)$$

with the introduced variables $A = \sum_{r \in \mathcal{R}} Y^{(r)} b h_r$, $D = \sum_{r \in \mathcal{R}} Y^{(r)} b (z_r^3 - z_{r-1}^3)/3$, $\Xi^{(p)} = b \bar{\epsilon}_{31}$ and $\Pi^{(p)} = b \bar{\epsilon}_{31} (z_p + z_{p-1})/2$. It must be noted that Eqs. (E.3) do not show a linear bending-membrane coupling, since only symmetric structures with regard to the neutral fiber are considered here. The internal forces are potentially discontinuous at the limits of the piezoelectric patches, due to the dependence of the variables $A, D, \Xi^{(p)}$ and $\Pi^{(p)}$ on the stratification of the structure. The electric charge is obtained by integrating Eq. (E.2b) on the upper electrodes. By considering the expression of the strain (Eq. (E.1)), it leads to:

$$Q^{(p)} = -\Xi^{(p)} [u]_0^L - \frac{\Xi^{(p)}}{2} \int_0^L (w_{,x})^2 dx + \Pi^{(p)} [w_{,x}]_0^L + C^{(p)} V^{(p)}. \quad (E.4)$$

with the capacity $C^{(p)} = \bar{\epsilon}_{33} b (x_+^{(p)} - x_-^{(p)})/h_p$. The equilibrium equations write:

$$m \ddot{u} - N_{,x} = n(x, t), \quad (E.5a)$$

$$m \ddot{w} - M_{,xx} - (N w_{,x})_{,x} = p(x, t). \quad (E.5b)$$

with $m = \sum_{r \in \mathcal{P}} \rho^{(r)} b h_r$ the mass per unit length, N the axial force and M the bending moment. $p(x, t)$ denotes the transverse forces per unit length, we assume that no external axial force is applied on the structure. Introducing the expressions of the internal forces (Eqs. (E.3)) in Eqs. (E.5) leads to:

$$m\ddot{u} - \left(A \left[u_{,x} + \frac{1}{2} w_x^2 \right] \right)_{,x} - \sum_{p \in \mathcal{P}} \left(\Xi^{(p)} \Delta^{(p)} \right)_{,x} V^{(p)} = n(x, t) \quad (\text{E.6alphequation})$$

$$m\ddot{w} + (Dw_{,xx})_{,xx} - A \left[u_x w_x + \frac{(w_x)^3}{2} \right]_{,x} + \sum_{p \in \mathcal{P}} \left(\left[\Pi^{(p)} \Delta^{(p)} \right]_{,xx} + \left[w_x \Xi^{(p)} \Delta^{(p)} \right]_{,x} \right) V^{(p)} = p(x, t) \quad (\text{E.6alphequation})$$

where $\Delta^{(p)}(x) = H(x - x_+) - H(x - x_-)$ and H is the Heaviside function. Eqs. (E.6) represent the (u, w) -formulation of the problem.

The transverse and axial displacements are now respectively expanded on N_w transverse modes ϕ_k and N_u axial modes ψ_s of the system with short-circuited patches. It writes $w(x, t) = \sum_{k=1}^{N_w} \phi_k(x) x_k(t)$ and $u(x, t) = \sum_{s=1}^{N_u} \psi_s(x) \eta_s(t)$, with x_k and η_s the modal coordinates of the transverse and axial modes. The modes are solutions to the following eigenvalue problems, related to the linear parts of Eqs. (E.6alphequation) and (E.6alphequation):

$$[D\phi_{k,xx}]_{,xx} - m\omega_k^2 \phi_k = 0, \quad [A\psi_{s,x}]_{,x} + m\gamma_s^2 \psi_s = 0 \quad (\text{E.7})$$

with ω_k and γ_s the eigenfrequencies. These modes present the following orthogonality properties:

$$\int_0^L m \phi_i \phi_j dS = \bar{m}_i \delta_{ij}, \quad \int_0^L m \psi_p \psi_s dS = \bar{m}_p \delta_{ps}, \quad (\text{E.8})$$

and are normalized such that the modal masses $\bar{m}_i = \bar{m}_p = 1 \forall i \in [1, N_w], \forall p \in [1, N_u]$. By substituting these expansions in Eqs. (E.4) and (E.6), integrating Eqs. (E.6) over the length of the beam and using the orthogonality properties, the modal equations of the complete electromechanical system are obtained. In the case of unmovable boundary conditions in the axial direction, we directly obtain the same equations as Eqs. (19a), (19b) and (19c), with the following expressions of the nonlinear coefficients $(a_{ij}^s, a_{si}^k, b_{ijl}^k)$:

$$a_{ij}^s = - \int_0^L \psi_s [A \phi_{i,x} \phi_{j,x}]_{,x} dx, \quad a_{si}^k = - \int_0^L \phi_k [A \psi_{s,x} \phi_{i,x}]_{,x} dx, \quad (\text{E.9a})$$

$$b_{ijl}^k = - \frac{1}{2} \int_0^L \phi_k [A \phi_{i,x} \phi_{j,x} \phi_{l,x}]_{,x} dx \quad \text{for } i, j, l, k \in [1, N_w], \text{ and } s \in [1, N_u].$$

The modal coupling coefficients $\varphi_i^{(p)}$ and parametric coefficients $\Lambda_{ik}^{(p)}$ write:

$$\chi_k^{(p)} = -\Xi^{(p)} [\phi_{k,x}]_{,x}^{(p)} dx \quad \forall k \in [1, N_w], \quad \gamma_s^{(p)} = -\Pi^{(p)} [\psi_{s,x}]_{,x}^{(p)} dx \quad \forall s \in [1, N_u],$$

$$\Lambda_{ik}^{(p)} = \Pi^{(p)} \int_0^1 \phi_{k,x} \phi_{i,x} dx. \quad (\text{E.10})$$

Finally, the modal forcing is defined by $F_k(t) = \int_0^L \phi_k(x) p(x, t) dx$.

References

- [1] Erturk A, Inman DJ. Piezoelectric energy harvesting. John Wiley & Sons; 2011.
- [2] Safaei M, Sodano HA, Anton SR. A review of energy harvesting using piezoelectric materials: state-of-the-art a decade later (2008–2018). *Smart Mater Struct* 2019;28(11):113001.
- [3] Trolier-McKinstry S, Muralt P. Thin film piezoelectrics for MEMS. *J Electroceram* 2004;12(1–2):7–17.
- [4] Gripp JAB, Rade DA. Vibration and noise control using shunted piezoelectric transducers: A review. *Mech Syst Signal Process* 2018;112:359–83.

- [5] Shivashankar P, Gopalakrishnan S. Review on the use of piezoelectric materials for active vibration, noise, and flow control. *Smart Mater Struct* 2020.
- [6] Preumont A. *Vibration control of active structures: an Introduction*. Springer; 2018.
- [7] Rhoads JF, Shaw SW, Turner KL. Nonlinear dynamics and its applications in micro-and nanoresonators. *Dynam Syst Control Conf* 2008;43352:1509–38.
- [8] Ramlan R, Brennan MJ, Mace BR, Kovacic I. Potential benefits of a non-linear stiffness in an energy harvesting device. *Nonlinear Dyn* 2010;59(4):545–58.
- [9] Daqaq MF, Masana R, Erturk A, Quinn D. On the role of nonlinearities in vibratory energy harvesting: a critical review and discussion. *Appl Mech Rev* 2014;66(4).
- [10] Soltani P, Kerschen G. The nonlinear piezoelectric tuned vibration absorber. *Smart Mater Struct* 2015;24(7):075015.
- [11] Lossouarn B, Deü J-F, Kerschen G. A fully passive nonlinear piezoelectric vibration absorber. *Philos Trans Royal Soc A: Math, Phys Eng Sci* 2018;376:20170142.
- [12] Muravyov AA, Rizzi SA. Determination of nonlinear stiffness with application to random vibration of geometrically nonlinear structures. *Comput Struct* 2003;81(15):1513–23.
- [13] Lacarbonara W, Yabuno H. Refined models of elastic beams undergoing large in-plane motions: theory and experiment. *Int J Solids Struct* 2006;43(17):5066–84.
- [14] Mignolet MP, Przekop A, Rizzi SA, Spottswood SM. A review of indirect/non-intrusive reduced order modeling of nonlinear geometric structures. *J Sound Vib* 2013;332:2437–60.
- [15] Givois A, Grollet A, Thomas O, Deü J-F. On the frequency response computation of geometrically nonlinear flat structures using reduced-order finite element models. *Nonlinear Dyn* 2019;97(2):1747–81.
- [16] Frangi A, Gobat G. Reduced order modelling of the non-linear stiffness in MEMS resonators. *Int J Non-Linear Mech* 2019;116:211–8.
- [17] Cusumano JP, Moon FC. Chaotic non-planar vibrations of the thin elastica, part 1: experimental observation of planar instability. *J Sound Vib* 1995;179(2):185–208.
- [18] Thomas O, Sénéchal A, Deü J-F. Hardening/softening behaviour and reduced order modelling of nonlinear vibrations of rotating cantilever beams. *Nonlinear Dynam* 2016;86(2):1293–318.
- [19] Guyomar D, Aurelle N, Eyraud L. Piezoelectric ceramics nonlinear behavior. Application to Langevin transducer. *J Phys III* 1997;7(6):1197–208.
- [20] Hajjaji A, Guyomar D, Touhtouh S, Pruvost S, Boughaleb Y, Rguiti M, Courtois C, Leriche A, Benkhouja K. Nonlinearity and scaling behavior in a soft lead zirconate titanate piezoceramic. *J Appl Phys* 2010;108(6):064103.
- [21] Leadenham S, Erturk A. Unified nonlinear electroelastic dynamics of a bimorph piezoelectric cantilever for energy harvesting, sensing, and actuation. *Nonlinear Dyn* 2015;79:1727–43.
- [22] Gatti CD, Febbo M, Machado SP, Osinaga S. A piezoelectric beam model with geometric, material and damping nonlinearities for energy harvesting. *Smart Mater Struct* 2020.
- [23] Frangi A, Opreni A, Boni N, Fedeli P, Carminati R, Merli M, Mendicino G. Nonlinear response of PZT-actuated resonant micromirrors. *J Microelectromech Syst* 2020.
- [24] Li H, Preidikman S, Balachandran B, Mote Jr CD. Nonlinear free and forced oscillations of piezoelectric microresonators. *J Micromech Microeng* 2006;16(2):356.
- [25] Thomas O, Mathieu F, Mansfield W, Huang C, Trolier-McKinstry S, Nicu L. Efficient parametric amplification in micro-resonators with integrated piezoelectric actuation and sensing capabilities. *Appl Phys Lett* 2013;102(16):163504.
- [26] Speciale A, Ardito R, Baù M, Ferrari M, Ferrari V, Frangi AA. Snap-through buckling mechanism for frequency-up conversion in piezoelectric energy harvesting. *Appl Sci* 2020;10(10):3614.
- [27] Saya D, Dezest D, Welsh AJ, Mathieu F, Thomas O, Leichlé T, Trolier-McKinstry S, Nicu L. Piezoelectric nanoelectromechanical systems integrating microcontact printed lead zirconate titanate films. *J Micromech Microeng* 2020;30:035004.
- [28] A.Sénéchal, O. Thomas, and J.-F. Deü. Optimization of shunted piezoelectric patches for vibration reduction of complex structures - application to a turbojet fan blade. In Proceedings of the ASME 2010 International Design Engineering Technical Conferences & Computers and Information in Engineering Conference, IDETC/CIE 2010, Montreal, Canada, August 2010.
- [29] Thierry O, De Smet O, Deü J-F. Vibration reduction of a woven composite fan blade by piezoelectric shunted devices. *J Phys: Conf Ser* 2016;744:012164.
- [30] Allik H, Hughes TJR. Finite element method for piezoelectric vibration. *Int J Numer Methods Eng* 1970;2(2):151–7.
- [31] V. Piefrot and A. Preumont. Finite element modeling of piezoelectric structures. In *Samtech User's Conference*, pages 1–17. Citeseer, 2001.
- [32] E. Balmès and A. Deraemaeker. Modeling structures with piezoelectric materials. SDT tutorial. <https://www.sdttools.com>, 2013.
- [33] Benjeddou A. Advances in piezoelectric finite element modeling of adaptive structural elements: a survey. *Comput Struct* 2000;76(1–3):347–63.
- [34] Mackerle J. Smart materials and structures—a finite element approach—an addendum: a bibliography (1997–2002). *Modell Simul Mater Sci Eng* 2003;11(5):707.
- [35] Vidal P, D'Ottavio M, Ben Thaïer M, Polit O. An efficient finite shell element for the static response of piezoelectric laminates. *J Intell Mater Syst Struct* 2011;22(7):671–90.

- [36] Cinefra M, Valvano S, Carrera E. A layer-wise MITC9 finite element for the free-vibration analysis of plates with piezo-patches. *Int J Smart Nano Mater* 2015;6(2):85–104.
- [37] Araújo AL, Carvalho VS, Soares CMM, Belinha J, Ferreira AJM. Vibration analysis of laminated soft core sandwich plates with piezoelectric sensors and actuators. *Compos Struct* 2016;151:91–8.
- [38] Ansys 18.0 documentation. ANSYS Inc., Canonsburgh, Pennsylvania, USA, 2017.
- [39] Abaqus documentation, version 6.14. Dassault Systèmes, Providence, RI, USA, 2016.
- [40] Collet M, Cunefare KA. Modal synthesis and dynamical condensation methods for accurate piezoelectric systems impedance computation. *J Intell Mater Syst Struct* 2008;19(11):1251–69.
- [41] Thomas O, Deü J-F, Ducarne J. Vibrations of an elastic structure with shunted piezoelectric patches: efficient finite element formulation and electromechanical coupling coefficients. *Int J Numer Methods Eng* 2009;80(2):235–68.
- [42] Badel A, Lagache M, Guyomar D, Lefeuvre E, Richard C. Finite element and simple lumped modeling for flexural nonlinear semi-passive damping. *J Intell Mater Syst Struct* 2007;18(7):727–42.
- [43] Al-Ajmi MA, Benjeddou A. Damage indication in smart structures using modal effective electromechanical coupling coefficients. *Smart Mater Struct* 2008;17(3):035023.
- [44] Thomas O, Ducarne J, Deü J-F. Performance of piezoelectric shunts for vibration reduction. *Smart Mater Struct* 2012;21(1):015008.
- [45] O. Thomas, B. Legrand, and C. Fuinel. Optimization of length and thickness of smart transduction layers on beam structures for control and m/nems applications. In *ASME 2015 Conference on Smart Materials, Adaptive Structures and Intelligent Systems*. American Society of Mechanical Engineers Digital Collection, 2015.
- [46] ANSI/IEEE Standard. IEEE Standard on piezoelectricity. pages 176–1987, 1988.
- [47] Toftækær JF, Benjeddou A, Høgsberg J. General numerical implementation of a new piezoelectric shunt tuning method based on the effective electromechanical coupling coefficient. In: *Mech Adv Mater Struct*. p. 1–15.
- [48] Lazarus A, Thomas O, Deü J-F. Finite element reduced order models for nonlinear vibrations of piezoelectric layered beams with applications to NEMS. *Finite Elem Anal Des* 2012;49:35–51.
- [49] Vizzaccaro A, Givois A, Longobardi P, Shen Y, Deü J-F, Salles L, Touzé C, Thomas O. Non-intrusive reduced order modelling for the dynamics of geometrically nonlinear at structures using three-dimensional finite elements. *Comput Mech* 2020.
- [50] Kuether RJ, Deane BJ, Hollkamp JJ, Allen MS. Evaluation of geometrically nonlinear reduced-order models with nonlinear normal modes. *AIAA J* 2015;53(11):3273–85.
- [51] Jain S, Tiso P, Rutzmoser JB, Rixen DJ. A quadratic manifold for model order reduction of nonlinear structural dynamics. *Comput Struct* 2017;188:80–94.
- [52] Mahdiabadi MK, Tiso P, Brandt A, Rixen DJ. A non-intrusive model-order reduction of geometrically nonlinear structural dynamics using modal derivatives. *Mech Syst Signal Process* 2021;147:107126.
- [53] Kim K, Radu AG, Wang XQ, Mignolet MP. Nonlinear reduced order modeling of isotropic and functionally graded plates. *Int J Non-Linear Mech* 2013;49:100–10.
- [54] Ponsioen S, Jain S, Haller G. Model reduction to spectral submanifolds and forced-response calculation in high-dimensional mechanical systems. *J Sound Vib* 2020;488:115640.
- [55] Touzé C, Thomas O, Chaigne A. Hardening/softening behaviour in non-linear oscillations of structural systems using non-linear normal modes. *J Sound Vib* 2004;273(1–2):77–101.
- [56] Y. Shen, N. Kesmia, C. Touzé, A. Vizzaccaro, L. Salles, and O. Thomas. Predicting the type of nonlinearity of shallow spherical shells: Comparison of direct normal form with modal derivatives. In *Proc. of NODYCON 2021 - second International Nonlinear Dynamics Conference*, Roma, Italy, February 2021.
- [57] Vizzaccaro A, Shen Y, Salles L, Blahos J, Touzé C. Direct computation of nonlinear mapping via normal form for reduced-order models of finite element nonlinear structures. In: *Comput Methods Appl Mech Eng*, submitted for publication.
- [58] Shen Y, Béreux N, Frangi A, Touzé C. Reduced order models for geometrically nonlinear structures: assessment of implicit condensation in comparison with invariant manifold approach. *Eur J Mech A/Solids* 2021;86:104165.
- [59] Vizzaccaro A, Salles L, Touzé C. Comparison of nonlinear mappings for reduced-order modeling of vibrating structures: normal form theory and quadratic manifold method with modal derivatives. *Nonlinear Dyn* 2020.
- [60] Shen Y, Vizzaccaro A, Kesmia N, Yu T, Salles L, Thomas O, Touzé C. Comparison of reduction methods for finite element geometrically nonlinear beam structures. *Vibration* 2021;4:175–204.
- [61] Touzé C, Vidrascu M, Chapelle D. Direct finite element computation of nonlinear modal coupling coefficients for reduced-order shell models. *Comput Mech* 2014;54(2):567–80.
- [62] V. Vyas, X.Q. Wang, A. Jain, and M.P. Mignolet. Nonlinear geometric reduced order model for the response of a beam with a piezoelectric actuator. In *56th AIAA/ASCE/AHS/ASC Structures, Structural Dynamics, and Materials Conference*, page 0692, 2015.
- [63] Opreni A, Boni N, Carminati R, Frangi A. Analysis of the nonlinear response of piezo-micromirrors with the harmonic balance method. *Actuators* 2021;10(2):21.
- [64] Holzapfel AG. *Nonlinear Solid Mechanics: A Continuum Approach for Engineering Science*. J. Wiley & Sons; 2000.
- [65] Dorfmann L, Ogden RW. *Nonlinear Theory of Electroelastic and Magnetoelastic Interactions*. Springer; 2014.
- [66] Ogden RW. *Non-Linear Elastic Deformations*. Dover; 1997.
- [67] Touzé C, Thomas O. Non-linear behaviour of free-edge shallow spherical shells: effect of the geometry. *Int J Non-linear Mech* 2006;41(5):678–92.
- [68] Gérardin M, Rixen D. *Mechanical Vibrations: Theory and Applications to Structural Dynamics*. 3rd ed. J. Wiley & Sons; 2015.
- [69] Bernadou M, Haenel C. Modelization and numerical approximation of piezoelectric thin shells. Part II: Approximation by finite element methods and numerical experiments. *Comput Methods Appl Mech Eng* 2003;192(37–38):4045–73.
- [70] Wang SY. A finite element model for the static and dynamic analysis of a piezoelectric bimorph. *Int J Solids Struct* 2004;41(15):4075–96.
- [71] Rizzi SA, Przekop A. System identification-guided basis selection for reduced-order nonlinear response analysis. *J Sound Vib* 2008;315(3):467–85.
- [72] Reddy JN. *Mechanics of laminated composite plates and shells: theory and analysis*. Wiley; 1997.
- [73] Mehner JE, Gabbay LD, Senturia SD. Computer-aided generation of nonlinear reduced-order dynamic macromodels-ii: Stress-stiffened case. *J Microelectromech Syst* 2000;9(2):270–8.
- [74] Cochelin B, Damiel N, Potier-Ferry M. *Méthode asymptotique numérique*. Hermès Lavoissier 2007.
- [75] L. Guillot, A. Lazarus, O. Thomas, C. Vergez, and B. Cochelin. A purely frequency based floquet-hill formulation for the efficient stability computation of periodic solutions of ordinary differential systems. *Journal of Computational Physics*, page 109477, 2020.
- [76] Lazarus A, Thomas O. A harmonic-based method for computing the stability of periodic solutions of dynamical systems. *Comptes Rendus Mécanique* 2010;338(9):510–7.
- [77] PI Ceramic, Open Source on <http://fisica.cab.cnea.gov.ar/bt/images/d/d3/PICat.pdf> (Accessed: 25-03-2020).
- [78] A. Sénéchal. Réduction de vibrations de structure complexe par shunts piézoélectriques. Application aux turbomachines. PhD thesis, Conservatoire National des Arts et Métiers, Paris, France, 2011.
- [79] Toftækær JF, Benjeddou A, Høgsberg J, Krenk S. Optimal piezoelectric resistive-inductive shunt damping of plates with residual mode correction. *J Intell Mater Syst Struct* 2018;29(16):3346–70.
- [80] Bruno BP, Fahmy AR, Stürmer M, Wallrabe U, Wapler MC. Properties of piezoceramic materials in high electric field actuator applications. *Smart Mater Struct* 2019;28:015029.
- [81] Johnk CTA. *Engineering electromagnetic fields and waves*. New York, John Wiley and Sons Inc; 1975. 667 p., 1975.
- [82] Rahmoune M, Benjeddou A, Ohayon R, Osmont D. New thin piezoelectric plate models. *J Intell Mater Syst Struct* 1998;9(12):1017–29.
- [83] Noliac group, <http://www.noliac.com/>. Piezo materials, Ver1404.
- [84] Ducarne J, Thomas O, Deü J-F. Placement and dimension optimization of shunted piezoelectric patches for vibration reduction. *J Sound Vib* 2012;331(14):3286–303.